Aslı TİKTAŞ

IZMIR KATIP CELEBI UNIVERSITY

2020

**IZMIR KATIP CELEBI UNIVERSITY**
**GRADUATE SCHOOL OF NATURAL AND APPLIED SCIENCES**

# PINNING AND DEPINNING OF DROPLETS AROUND STEP GEOMETRIES

**M.Sc. THESIS**
**Aslı TİKTAŞ**

**Department of Mechanical Engineering**

**Thesis Advisor: Asst. Prof. Dr. Umut CEYHAN**

**JUNE 2020**

**IZMIR KATIP CELEBI UNIVERSITY**
**GRADUATE SCHOOL OF NATURAL AND APPLIED SCIENCES**

# PINNING AND DEPINNING OF DROPLETS AROUND STEP GEOMETRIES

**M.Sc. THESIS**

**Aslı TİKTAŞ**
**(Y180217003)**

**Department of Mechanical Engineering**

**Thesis Advisor: Asst. Prof. Dr. Umut CEYHAN**

**JUNE 2020**

İZMİR KATİP ÇELEBİ ÜNİVERSİTESİ
FEN BİLİMLERİ ENSTİTÜSÜ

# DAMLACIKLARIN BASAMAK GEOMETRİLERİ ETRAFINDA TUTUNMASI VE KURTULMASI

**YÜKSEK LİSANS TEZİ**
**Aslı TİKTAŞ**
**(Y180217003)**

**Makine Mühendisliği Ana Bilim Dalı**

**Tez Danışmanı: Dr. Öğr. Üyesi Umut CEYHAN**

**HAZİRAN 2020**

**Aslı TİKTAŞ**, a **M.Sc.** student of **IKCU Graduate School Of Natural And Applied Sciences**, successfully defended the thesis entitled "PINNING AND DEPINNING OF DROPLETS AROUND STEP GEOMETRIES", which she prepared after fulfilling the requirements specified in the associated legislations, before the jury whose signatures are below.

**Thesis Advisor :**

**Asst. Prof. Dr. Umut CEYHAN** ........................ Umut Ceyhan
İzmir Kâtip Çelebi University

**Jury Members :**

**Assoc. Prof. Dr. Alpaslan TURGUT** ........................
Dokuz Eylül University

**Asst. Prof. Dr. Ziya Haktan KARADENİZ** ........................
İzmir Kâtip Çelebi University

**Date of Defense :** 25.06.2020

***To my family***

# FOREWORD

First and foremost, I would like to thank my advisor, Asst. Prof. Dr. Umut CEYHAN. Whenever I encounter a problem about my research or writing, his office door was always open and he supported me every time. Also I thank my parents for their endless support and encouragement through the duration of researching and writing this thesis.

June 2020

Aslı TİKTAŞ

# TABLE OF CONTENTS

# LIST OF TABLES

**Page**

# LIST OF FIGURES

# NOMENCLATURE

$A$: Droplet volume per unit depth

$Bo$: Bond number

$Ca$: Capillary number

$f$: Film thickness

$\boldsymbol{f}$: Force vector

$f_0$: Precursor film thickness

$g$: Gravitational acceleration

$h$: Substrate topography function

$h_s$: Step height

$\boldsymbol{i}$: Unit vector along $x$-coordinate

$\boldsymbol{j}$: Unit vector along y-coordinate

$L$: Domain length

$\boldsymbol{n}$: Unit outward normal at the interface

$p$: Pressure

$q$: Volume flow per unit depth

$r_0$: Initial radius of curvature

$S$: Spreading parameter

$t$: Time

$u$: $x$-component of velocity

$V$: Speed

$v$: Droplet volume

$x$: $x$-coordinate

$y$: $y$-coordinate

Greek Letters

$\alpha$: Substrate inclination angle

$\eta$: Fluid dynamic viscosity

$\gamma$: Surface tension between interfaces

$\lambda$: Step steepness parameter

$\Pi$: Disjoining pressure

$\zeta$: Interface measured from horizontal

Subscripts

$A$: Advancing

$c$: Critical

$cg$: Center of gravity

$CL$: Contact line

$e$: Equilibrium

$lv$: Liquid and vapor

$m$: Mesoscopic

$R$: Receding

$r$: Residual

$ret$: Retention

$s$: Step

$sl$: Solid and liquid

$sv$: Solid and vapor

Superscripts

$l$: Liquid

$s$: Solid

$v$: Vapor

~: Dimensional quantities

# PINNING AND DEPINNING OF DROPLETS AROUND STEP GEOMETRIES

## ABSTRACT

Droplets moving over inclined heterogenous substrates may pin around rough spots. A simplified model of one of these spots having a backward facing step geometry over a chemically homogeneous inclined substrate reveals that the step is responsible from the pinning-depinning of the leading edge of the droplet. We consider a two-dimensional partially wetting droplet and model its motion by the evolution equation with a precursor film model. The phase diagrams formed define pinning-depinning transition curves determined by a simple force balance of retention forces due to hysteresis, step and gravitational force. For fixed $Bo$ number and inclination, we show that it is the slope of the step that determines transition. The existence of the multiple steps, however, alters this transition as the receding contact line may pin at the steps and leave residual droplets behind. Also we show that multiple droplets may help from pinning to depinning due to the increase in effective $Bo$ number.

# DAMLACIKLARIN BASAMAK GEOMETRİLERİ ETRAFINDA TUTUNMASI VE KURTULMASI

## ÖZET

Eğimli heterojen substratlar üzerinde hareket eden damlacıklar pürüzlü noktaların etrafına tutunabilir. Kimyasal olarak homojen eğimli bir substrat üzerinde geriye dönük bir basamak geometrisine sahip olan bu pürüzlü noktalardan birinin basitleştirilmiş bir modeli, basamak geometrisinin damlacığın öncü temas çizgisinin tutunmasından sorumlu olduğunu ortaya koymaktadır. İki boyutlu kısmen ıslanan bir damlacığın hareketini öncü film modeli kullanan film ilerleme denklemi ile modelliyoruz. Oluşturduğumuz faz diyagramları; histerezis, basamak ve yerçekimi kuvveti nedeniyle tutma kuvvetlerinin basit bir kuvvet dengesi ile belirlenen tutunma/tutunmama geçiş eğrilerini tanımlamaktadır. Sabit *Bo* sayısı ve eğim için, bu geçiş basamak eğimince belirlenmektedir. Bununla birlikte birden fazla basamağın varlığı, bu geçişi geri çekilen temas çizgisinin basamağa tutunması veya basamağın arkasında artık damlacıklar bırakacak şeklinde değiştirir. Ayrıca etkin *Bo* sayısının artması nedeniyle çoklu damlacıkların tutunmadan tutunmamaya doğru yardımcı olabileceğini gösteriyoruz.

# 1. INTRODUCTION

Droplet motion is related to many industrial and technological applications and the understanding of the motion of droplets over surfaces related to these applications is crucial. The purpose may be obtaining clean surfaces, e.g. greenhouse covers [1] and car windows [2], [3], [4], or to keep droplets in place such as printing of electronics [5], [6], to promote the uphill droplet motion [7] or to increase the heat transfer efficiency [8], [9], [10].

Filtration [11], spraying [12], the formation of raindrops [13], agricultural coating applications [14] and inkjet printing process [15] include motion and coalescence of droplets. For example, line printing process includes coalescence of sessile drops and spreading. The shape and resolution of printed lines are determined by the motion of droplets. In this process, when the liquid droplets contact to one another, they are pulled together by surface tension force. The coalescence continues until reaching an equilibrium shape to minimize its surface energy. Agricultural spraying process, to provide protectant pesticides due to environmental considerations, on a leaf requires a uniform coating over the leaf surface. If there exists any surfactant on the leaf surface, however, lowers the contact angle of the spray droplets make with the surface and the fluid is able to cover the leaf surface.

Besides, many researchers have studied droplet motion in nature which they have become later inspiration for the design of new materials or structures [16], [17], [18], [19], [20]: for instance, Namib Desert beetles harvest droplets from the fog-laden by tilting their body towards the wind. Their wing surface consists of combined hydrophilic and hydrophobic bumps which allow them to coalesce small droplets into the bigger ones inside the fog to obtain drinking water [21], [22]. Similarly, the structure of the mosquito eyes (C. pipiens) has superhydrophobic anti-fogging property for maintaining a clear vision in dark areas. The re-entrant structures observed on the surface of lotus leaves have been discovered to be responsible from the unexpectedly high repellency. Surfaces having reentrant curvatures [23], [24], [25] allowing oleophobicity encounter pinning and depinning of the contact lines around some topographical heterogeneities. These structures let even the very low-energy liquids suspend and generate superrepellent substrates which can be used for oil-water seperation, electronics cooling by nucleate boiling, etc.

In most of the aforementioned examples, the motion of droplets is susceptible to topographical and/or chemical heterogeneities which result in non-unique contact angles the droplet makes with the surface. To understand the behaviour of contact lines around structured substrates, we study the motion of droplets around inclined steps. The simple step structure allows us to mimic throughs and peaks.

When a droplet meets the substrate, the triple line meets the substrate at an angle and the equilibrium interface takes spherical cap form in the absence of gravity to minimize its surface energy. A representative two-dimensional droplet sitting on a flat substrate is shown in figure 1.1.

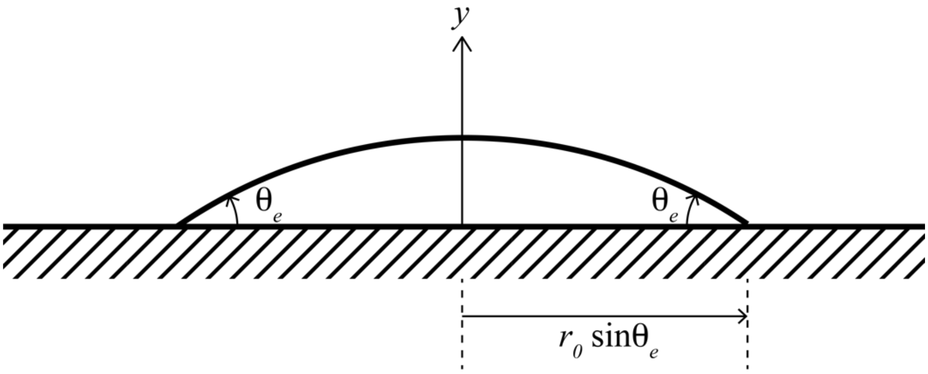

**Figure 1.1** Two dimensional droplet sitting over a flat substrate.

For atomically smooth and chemically homogeneous substrates, Young [26] developed an equation in order to relate equilibrium contact angle and surface energies at the interfaces by balancing tangential components of the surface energies at the three phase contact line. The equilibrium contact angle on the ideal substrate is given by

$$\cos\theta_e = \frac{\gamma_{sv} - \gamma_{sl}}{\gamma_{lv}} \tag{1.1}$$

where $\gamma_{sv}$, $\gamma_{sl}$, $\gamma_{lv}$ are surface tensions at solid-vapor, solid-liquid and liquid-vapor interfaces, respectively and $\theta_e$ is the equilibrium contact angle.

When the substrate is not ideal, however, the contact angle deviates from its Young value. The measured advancing contact angle differs from the receding one, this difference is termed as contact angle hysteresis [27], [28], [29]. This can be due to chemical heterogeneity, roughness and adsorption into the surface which may alter the surface properties [30], [31]. Wenzel [32] developed an equation which includes contact angle, adhesion tension and surface tension of the wetted interface for chemically homogeneous but rough surfaces for a horizontal substrate by evaluating surface roughness factor and he observed that wetted area increases gradually during spreading process and it decreases the specific energy of the interface and rate of the decrease is rapid for rough surfaces. Let the differential surface energy variation per unit depth be $dW$ due to the displacement of the contact line at amount of $dx$. This variation has two contributions and defined as

$$dW = r(\gamma_{sv} - \gamma_{sl})dx - \gamma_{lv}\cos\theta^{*}dx \tag{1.2}$$

where $r$ is the roughness factor defines as ratio of real surface area to apparent surface area and $\theta^{*}$ is the apparent contact angle. In equation (1.2), this change due to creation of new interface is defined as the net contribution to the surface energies. In the limit as $dx \to 0$, $\frac{dW}{dx} \to 0$, which is the minimization of surface energy, the apparent contact angle is defined as

$$\cos\theta^{*} = rcos\theta_{e}. \tag{1.3}$$

For chemically heterogeneous surfaces, Cassie [33] developed an equation which includes apparent contact angle, adhesion tension and surface tension of the wetted and unwetted interfaces for chemically heterogeneous surfaces which by evaluating ratio of total wetted surface area to projected surface area to define apparent contact angle droplet makes with such substrate including air pockets. Let $\phi$ be the fraction of the projected area of the total projected area per depth of the wetted region and $1 - \phi$ be the fraction of the total projected area per depth of the unwetted region. Due to creation of new interfaces, the change in the surface energy per unit depth is then

$$dW = \phi r(\gamma_{sv} - \gamma_{sl})dx + (1-\phi)\gamma_{lv}dx - \gamma_{lv}\cos\theta^{*}dx. \qquad (1.4)$$

When $\phi \rightarrow 1$, this equation reduces to the Wenzel equation. In the limit as $dx \rightarrow 0$, the apparent contact angle in the Cassie state is defined as

$$\cos\theta^{*} = \phi r\cos\theta_e + (1-\phi). \qquad (1.5)$$

It is observed, however, that for the same roughness factor, the measured contact angles may differ due to different topography. The advancing and receding contact lines over pillars do not behave in the same way as pored structures [34]. The classical Wenzel-state or Cassie-Baxter state relations are not sufficient to explain this discepancy as they both use averaging quantities for the effective interface energy. The existence of sub-micron scale concave surfaces, for example, alter the contact angles and hysteresis [24]. A simple way of visualization of hysteresis is the observation of droplet motion over tilted surfaces. Over an inclined flat substrate, the balance between gravitational and surface tension forces determines the shape of droplet; while the former pushes the droplet down the incline, the latter pulls the droplet against the gravity due to a retention force. The droplet takes an asymmetric shape having contact angles different from the equilibrium contact angle $\theta_e$ on a flat substrate. When the critical inclination angle is achieved, the droplet moves over the substrate; the leading edge of the droplet advances with an advancing contact angle $\theta_A$ while its trailing edge recedes with an receding contact angle $\theta_R$ which is the dynamic component of the contact angle hysteresis originating from the droplet motion. The difference between these angles and Young angle depends on the Capillary number, $Ca$ is based on contact line speed defining the ratio of viscous forces to surface tension forces, and scales linearly with $Ca^{1/3}$ which is given by the Cox-Voinov law [35], [36]. The ratio of gravitational to surface tension forces defined by the Bond number, $Bo$, is a critical control variable on the motion and shape of the droplet over inclined surfaces. The competing force between gravity and interfacial forces causing retention due to contact angle hysteresis determines both the shape and the motion. Furmidge [28], Macdougall and Ockrent [37] experimentally show that there exists a critical inclination angle, $\alpha_c$, at which a droplet starts moving, i.e. whenever the gravitational force acting on the droplet is equal or greater than the contact line retention forces due to surface tensions, it moves. This condition is provided by the tangential force balance acting on a droplet over a flat substrate and given by

$$\cos\theta_R - \cos\theta_A = \frac{\rho g A}{\gamma} sin\alpha_c = Bosin\alpha_c. \tag{1.6}$$

In equation (1.6), $A$ is droplet volume per unit depth for a two-dimensional droplet, $\rho$ is the liquid density, $g$ is the gravitational acceleration and $\gamma$ is the surface tension between liquid and vapor. Different variations of equation (1.6) are proposed to a specific problem and are validated by others [38], [39]. For small $Bo\sin\alpha$ values, the two-dimensional droplets take almost circular arc shape, beyond a critical inclination angle, however, e.g. for fixed $Bo$, the droplet undergoes a wetting transition resulting with an elongated profile and completing this transition, it moves with a terminal speed [29], [40], [41].

The first problem in the modelling the motion of droplets over surfaces is the contact line singularity at the moving three phase contact lines. When a droplet moves over a surface, the no-slip boundary condition, which is a common usage for hydrodynamic approach, requires a moving viscous fluid to stick to the surface and the contact line has zero speed at this solid surface, if stationary. It is observed, e.g. in coating processes and wetting films, that three phase contact line (solid, liquid, and gas) advances or recedes, in other words contact line is not static and there is a contradiction which violates the no–slip condition since displaced fluid particles at the contact line must move relative to the solid surface. Also this boundary condition cause nonintegrable shear stress and viscous dissipation at the vicinity of three phase contact line. Therefore, singularity at the contact line needs to be alleviated for proper investigation of contact line motion [42], [43]. Many mechanisms for relieving the dynamical singularity at the contact line region have been suggested and used in many studies, however, only some of them will be included for brevity. One of the relieving methods is slip models [41], [44], [45] where the no–slip condition is replaced by some type of slip boundary condition. Dussan et al. [46]

show that to alleviate the singularity and predict some measurable physical quantities, multi–valued velocity near the triple line has to be relieved simultaneously which can be done by using any slip coefficient. The origin of the slip velocity adjacent to the contact line and its theoretical analysis are given in Ruckenstein and Dunn [47].

Another singularity alleviation method at the moving contact line is that the triple line is replaced with an apparent one and connected to a precursor film of constant thickness in front of the contact line at the mesoscopic length scale. At this scale, the molecular interactions matter: there exists a disjoining pressure $\Pi(f)$ [48], where $f$ is the film thickness, with various models such as the ones derived from van der Waals forces [49], [50] or diffuse interface models [51]. If liquid film thickness is smaller than 100 nanometer, intermolecular forces due to attractive and repulsive interactions of liquid, solid and air molecules involving thin film exists apart from gravitational forces, capillary forces and surface tension forces and these forces per unit area is called as disjoining pressure isotherm which has three possible components. These components are van der Waals due to interaction of dipole molecules, electrostatic due to interaction of electrostatic layers under the thin liquid film and steric components due to interaction between liquid film surface and large molecules involved in this surface. Hamakar [52] compute London van der Waals forces between two sphere particles and details of this computation are given in Appendix A. Schwartz and Elley propose a disjoining pressure model which includes an power relation of disjoining pressure and film thickness according to basis of London van der Waals forces and given by

$$\Pi = \frac{B}{{f_0}^n}\left[\left(\frac{f_o}{f}\right)^n - \left(\frac{f_0}{f}\right)^m\right] \tag{1.7}$$

where $B$ is a positive constant, $n$ and $m$ are exponents and $f_0$ is the precursor film thickness. Also they express that if a point which are taken from partially wetting system is far enough from the solid substrate, the contribution of London van der Waals component on disjoining pressure decreases, then it can be neglected. So in this state, we can determine Hamakar constant in terms of exponentials in the disjoining pressure model and critical equilibrium contact angle by applying tangential force balance approach on the triple line. Because this state satisfy thermodynamically equilibrium condition and stability of thin film.

$$B = {f_0}^{n-1}\left(\frac{(n-1)(m-1)}{2(n-m)}\right)\gamma {\theta_e}^2. \tag{1.8}$$

To see the difference between slip and precursor models, Savva&Kalliadasis [53], Sibley et.al. [54] investigate these two models and constitute a connection between them by analyzing the contact line motion of two–dimensional spreading droplets. For spreading parameter $S < 0$ (partial wetting), Navier–slip model and Ruckenstein-Dunn model are taken for slip condition; whereas for the precursor film model, the disjoining pressure term is taken separately for van der Waals model and Sharma model. Their study show that modification of the model equations for precursor and slip model leads to equivalent quasi–static limit which is a sign of same dynamics for different models.

The motion of droplets on either inclined or rough surfaces needs a similar treatment of the advancing and receding contact lines. Savva & Kalliadasis [41], [55] work on two dimensional droplets on heterogeneous surfaces (including both chemical and topographical) by addressing both horizontal and inclined surfaces. Using lubrication approximations, they model the droplet motion with a slip boundary condition. They review the static and dynamic behavior of the droplet motion and use a singular perturbation method in order to evaluate position of the moving drops. Without imposing the hysteresis effect a priori, equilibrium of droplets cannot be preserved over ideal surfaces, however, droplets can reach its equilibrium on the substrate having heterogeneities. They also review, the effect of topographical and chemical heterogeneities on the critical angle, for periodic, single–wavelength and small–amplitude heterogeneities.

Thiele [40] revise the analysis of the evolution of a two and three–dimensional thin liquid films over tilted surfaces. In their model, they include a disjoining pressure which is formulated by a diffuse interface theory. They show that if inclination angle increases, so does the speed of the contact line and diffuse interface thickness increases and it provides formation of a thinner drop and stronger oscillations.

When the surfaces have topographical heterogeneities, the motion also depends on the defect parameters which may either cause the droplet to stick to it, or delay its motion. Park&Kumar [56] study on two–dimensional droplet, advancing over a surface having  a single defect tilted at a certain angle measured from their level surface. Unlike Savva &  Kalliadasis (2013), who work on the behaviour of droplets on tilted heterogeneous surfaces  having periodic structures,  focus on a single topographical defect  of Gaussian shape over a flat tilted substrate to examine the influence of pinning at the  defect by using lubrication equations utilizing precursor-film model. They numerically observe that droplet pinning occurs at the point which has a minimum slope on the defect surface. If retention force due to the hysteresis is bigger than sliding forces, droplet remains pinned at a non–zero sliding angle. At this configuration, advancing contact angle is maximum and retention forces are maximized. Although they argue the effects of defect width, height and slope separately, varying either width or height changes the defect slope. Also they show that residual droplet formation on the substrate by setting proper geometric parameters which are height and width of the step and they explain that residual formation occurs due to interaction of defect surface and receding meniscus when inclination angle is above of a critical value.

According to experimental study of Kalinin et.al. [57], pinning-depinning of a droplet is mostly determined by the slope of the topographical defect( the steepness of a step down of the rings with trapezoidal cross-sections), consistent with Gibbs inequality [58]. In general, as the slope of step increases, so does the apparent advancing angle. In other words, the strength of the pinning increases. Recently, Escobar et.al. [59] observe the contact line pinning at the side-walls of the concentric rings with which they explain the zipping-depinning mode of sessile microdroplets.

We want to show pinning-depinning transition of two-dimensional droplet motion on an inclined surface which includes topographical heterogeneities by using lubrication theory with a precursor film approximation. These topographical heterogeneities on the solid surface can be created with numerous steps ups and downs. Experimental studies showed that at the first time advancing edge of the droplet meets with maximum slope side of the defect surface and advancing edge moves faster with decreasing apparent contact angle. So, motion slows at receding edge of droplet in order to satisfy continuity of the motion. If retention forces dominate over the gravitational forces, droplet either pins or depins at this region. So we create topographical heterogeneities as the single backward facing step geometry and this simple geometry provides us explain this problem physically with all aspects and controllable slope with different step heights. We first study on pinning/depinning transition of the advancing side of the droplet. The phase diagrams of this transition reveal that the critical condition is determined by a simple force balance around the contact line of the droplet; the difference from the flat substrate is the retention force due the existence of topography change. The existence of roughness around the receding contact line, however, alters this transition as it may also pin at one of these spots and may leave residual droplets behind the forward-facing steps. Also we evaluate effect of multiple droplets on pinning-depinning trasition mechanism by considering effective $Bo$ number.

# 2. MODEL PROBLEM

We evaluate the motion of droplets over inclined substrates having step-like structures in plane using lubrication approximation with precursor film model. Figure 2.1 shows the schematic of the droplet over such an incline. We fix the coordinate at the substrate of level $y = 0$. Denoting the dimensional quantities with tilde mark $(\sim)$, we define the substrate by $\tilde{h}(\tilde{x})$ and the liquid-vapor interface of the droplet is defined by $\tilde{\zeta}(\tilde{x}, \tilde{t})$ measured from substrate level. The film thickness is defined as $\tilde{f} = \tilde{\zeta} - \tilde{h}$. Away from the contact lines, the precursor film thickness is $\tilde{f}_0$.

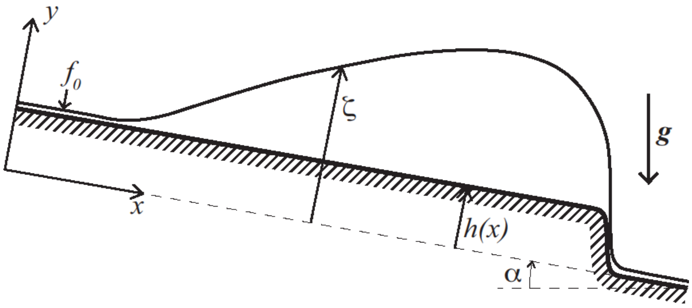

**Figure 2.1** Problem domain: droplet around an inclined step.

The substrate is inclined at an angle $\alpha$ as shown in figure 2.1 and gravitational acceleration $\boldsymbol{g} = g(\sin\alpha\boldsymbol{i} - \cos\alpha\boldsymbol{j})$ acts downwards. The topography is defined using hyperbolic tangent function.

$$\tilde{h}(\tilde{x}) = \frac{\tilde{h}_s}{2}\left[1 - \tanh\left(\frac{\tilde{x} - \tilde{x}_s}{\lambda}\right)\right] \tag{2.1}$$

where $h_s$ is the step height, $x_s$ is the $x$ coordinate of the maximum absolute slope location and $\lambda$ is the step steepness parameter; the smaller $\lambda$ is, the steeper the step.

We treat the fluid to be incompressible, Newtonian and non-volatile with uniform density $\rho$, dynamic viscosity $\eta$. We also treat the interfacial tension $\gamma$ to be uniform between the interfaces. The motion of droplet over the substrate is governed by the continuity and linear momentum equations, respectively:

$$\tilde{\nabla} \cdot \tilde{\boldsymbol{u}} = 0, \tag{2.2}$$

$$\rho \left( \frac{\partial \tilde{\boldsymbol{u}}}{\partial \tilde{t}} + \tilde{\boldsymbol{u}} \cdot \tilde{\nabla} \tilde{\boldsymbol{u}} \right) = -\tilde{\nabla} \tilde{p} + \eta \tilde{\nabla}^2 \tilde{\boldsymbol{u}} + \rho g. \tag{2.3}$$

Here $\tilde{\boldsymbol{u}}$ is the velocity vector defined in plane as $\tilde{\boldsymbol{u}} = \tilde{u}\boldsymbol{i} + \tilde{v}\boldsymbol{j}$. For slender droplets and $Re \ll 1$, we obtain lubrication equations (see Appendix B), the continuity is not altered, but the momentum equation (2.3), in its component form, reduces to

$$\frac{\partial \tilde{p}}{\partial \tilde{x}} = \eta \frac{\partial^2 \tilde{u}}{\partial \tilde{y}^2} + \rho g \sin\alpha, \tag{2.4}$$

$$\frac{\partial \tilde{p}}{\partial \tilde{y}} = -\rho g \cos\alpha. \tag{2.5}$$

The $\tilde{x}$-component of the film velocity can be obtained by integrating the $\tilde{x}$-momentum in $\tilde{y}$. Here, we should note that $\frac{\partial \tilde{p}}{\partial \tilde{x}}$ is not a function of $\tilde{y}$ as seen from equation (2.4). The velocity profile satisfying the no-slip at $\tilde{y} = \tilde{h}$ and vanishing shear stress at $\tilde{y} = \tilde{\zeta}$ is found to be

$$\tilde{u} = \frac{1}{\eta} \left( \frac{\partial \tilde{p}}{\partial \tilde{x}} - \rho g \sin\alpha \right) \left( \frac{\tilde{y}^2}{2} - \tilde{\zeta}\tilde{y} - \frac{\tilde{h}^2}{2} + \tilde{\zeta}\tilde{h} \right). \tag{2.6}$$

Here $\tilde{p}$ is the pressure and we determine its gradient using the normal force balance at the interface. Volume flow rate per unit depth, $\tilde{q}$, across the film thickness $\tilde{f}$ is computed by integrating the velocity profile $\tilde{u}$ from $\tilde{y} = \tilde{h}$ to $\tilde{y} = \tilde{\zeta}$:

$$\tilde{q} = -\frac{1}{3\eta} \left( \frac{\partial \tilde{p}}{\partial \tilde{x}} - \rho g \sin\alpha \right) \left( \tilde{\zeta} - \tilde{h} \right)^3. \tag{2.7}$$

The interfacial momentum balance in the normal direction determines the pressure difference at the interface to be

$$\tilde{p}^l - \tilde{p}^v = \gamma \widetilde{\boldsymbol{\nabla}} \cdot \boldsymbol{n} - \tilde{\Pi}. \tag{2.8}$$

In equation (2.8), $\tilde{p}^l$ and $\tilde{p}^v$ are the interface liquid and vapor pressures, respectively. $\boldsymbol{n}$ is the unit outward normal at the interface and $\tilde{\Pi}$ is the disjoining pressure. For small slope interface the surface force due to variation of $n$ reduces to $\widetilde{\boldsymbol{\nabla}} \cdot \boldsymbol{n} = -\frac{\partial^2 \zeta}{\partial x^2}$ (see Appendix C).

The pressure distribution within the fluid is obtained by integrating $\tilde{y}$ momentum given in equation (2.5) as

$$\tilde{p} = -\rho g \tilde{y} \cos\alpha + z(\tilde{x}). \tag{2.9}$$

In equation (2.9), $z(\tilde{x})$ is found by evaluating the pressure at the interface and using equation (2.8) as

$$z(\tilde{x}) = \tilde{p}^v + \gamma \widetilde{\boldsymbol{\nabla}} \cdot \boldsymbol{n} - \tilde{\Pi} + \rho g \tilde{\zeta} \cos\alpha. \tag{2.10}$$

If we combine equations (2.9) and (2.10) and assume vapor pressure to be uniform along the interface, the $\tilde{x}$ derivative of the pressure reduces to

$$\frac{\partial \tilde{p}}{\partial \tilde{x}} = -\gamma \frac{\partial^3 \tilde{\zeta}}{\partial \tilde{x}^3} - \frac{\partial \tilde{\Pi}}{\partial \tilde{x}} + \rho g \frac{\partial \tilde{\zeta}}{\partial \tilde{x}} \cos\alpha. \tag{2.11}$$

We replace the pressure gradient term in equation (2.7) with above and rewrite as

$$\tilde{q} = -\frac{1}{3\eta} \left( -\gamma \frac{\partial^3 \tilde{\zeta}}{\partial \tilde{x}^3} - \frac{\partial \tilde{\Pi}}{\partial \tilde{x}} + \rho g \frac{\partial \tilde{\zeta}}{\partial \tilde{x}} \cos\alpha - \rho g \sin\alpha \right) \left( \tilde{\zeta} - \tilde{h} \right)^3. \tag{2.12}$$

The film evolution (see Appendix D) is governed by

$$\frac{\partial \tilde{f}}{\partial \tilde{t}} + \frac{\partial \tilde{q}}{\partial \tilde{x}} = 0 \tag{2.13}$$

and using the definition of $\tilde{q}$ in equation (2.12), we obtain the evolution equation of the film thickness $f$:

$$\frac{\partial \tilde{f}}{\partial \tilde{t}} + \frac{\partial}{\partial \tilde{x}}\left[\begin{matrix} -\frac{\tilde{f}^3}{3\eta}\left(\rho g\left(\frac{\partial\left(\tilde{f}+\tilde{h}\right)}{\partial \tilde{x}}\cos\alpha - \sin\alpha\right)\right) \\ -\gamma\frac{\partial^3\left(\tilde{f}+\tilde{h}\right)}{\partial \tilde{x}^3} - \frac{\partial\tilde{\Pi}}{\partial \tilde{x}} \end{matrix}\right] = 0. \tag{2.14}$$

Because we initiate the droplet motion considering its shape to be a circular arc sitting over a flat substrate, we first define the geometry of the intial droplet as shown in figure 1.1. The radius of curvature of the initial droplet is $r_0$, the equilibrium contact angle the droplet makes with the substrate is $\theta_e$. From geometry, the characteristic height of the droplet is $h_0 = r_0(1-\cos\theta_e)$ and characteristic length of the droplet is $l_0 = r_0 sin\theta_e$; the volume per unit depth of the droplet is $A = {r_0}^2(\theta_e - \sin\theta_e)$. For small equilibrium contact angles, the droplet is slender: $\frac{h_0}{l_0} = \frac{r_0 cos(1-\cos\theta_e)}{r_0 sin\theta_e} \ll 1$.

We non-dimensionalize equation (2.14) using the following scales:

$$x^s = \left[\frac{\tilde{A}\sin^2\theta_e}{\theta_e - \sin\theta_e\cos\theta_e}\right]^{1/2}, \tag{2.15}$$

$$f^s = \left[\frac{\tilde{A}(1-\cos\theta_e)^2}{\theta_e - \sin\theta_e\cos\theta_e}\right]^{1/2}, \tag{2.16}$$

$$u^s = \frac{\gamma(1-\cos\theta_e)^3}{3\eta\sin^3\theta_e}, \tag{2.17}$$

$$t^s = \frac{3\eta\sin^3\theta_e}{\gamma(1-\cos\theta_e)^3}\left[\frac{\tilde{A}\sin^2\theta_e}{\theta_e - \sin\theta_e\cos\theta_e}\right]^{1/2}, \tag{2.18}$$

$$p^s = \gamma \left[\frac{(1-\cos\theta_e)^2}{\tilde{A}\sin^4\theta_e}\right]^{1/2} \frac{3\eta\sin^3\theta_e}{\gamma(1-\cos\theta_e)^3}\left[\frac{A\sin^2\theta_e}{\theta_e-\sin\theta_e\cos\theta_e}\right]^{1/2}. \tag{2.19}$$

The non-dimensional evolution of the film, the tilde (~) mark is now dropped for dimensionless quantities, is then governed by

$$\frac{\partial f}{\partial t}+\frac{\partial}{\partial x}\left[\begin{array}{c} -f^3\left(Bo\left(\cos\alpha\dfrac{\partial(f+h)}{\partial x}-E\right)\right) \\ -\gamma\dfrac{\partial^3(f+h)}{\partial x^3}-\dfrac{\partial\Pi}{\partial x}\end{array}\right]=0 \tag{2.20}$$

where $E=\frac{\sin\alpha\sin\theta_e}{1-\cos\theta_e}$ and $Bo$ is the Bond number defining the ratio of gravitational to surface tension forces and defined as $Bo=\frac{\rho g(x^s)^2}{\gamma}$. The boundary conditions are

$$f(0,t)=f_0, \tag{2.21}$$

$$f(L,t)=f_0, \tag{2.22}$$

$$\frac{\partial f(0,t)}{\partial x}=0, \tag{2.23}$$

$$\frac{\partial f(L,t)}{\partial x}=0. \tag{2.24}$$

While the boundary conditions (2.21-2.24) define that the film goes to the precursor film thickness of $f_0$ away from the droplet with the end points defined at $x=0$ and $x=L$, they enforce the film thickness to be uniform away from the droplet.

The non-dimensional form of the disjoining pressure model is

$$\Pi=\hat{\mathrm{A}}\left[\left(\frac{f_0}{f}\right)^m-\left(\frac{f_0}{f}\right)^n\right] \tag{2.25}$$

where Â is known as Hamakar constant defined as

$$\hat{A} = \frac{1}{f_0}\left(\frac{\theta_e \sin\theta_e}{1 - \cos\theta_e}\right)^2 \frac{(m-1)(n-1)}{2(m-n)}. \tag{2.26}$$

The choice of the parameters $m$ and $n$ in this two –term disjoining pressure model affects the solution. Common choices for the parameters are the pairs $(m, n) = (3,2)$, $(m, n) = (4,3)$ and $(m, n) = (9,3)$. The last two pairs increase Hamakar constant to $3\hat{A}$ and $4/3\hat{A}$, respectively, for fixed $f_0$ and $\theta_e$. When Â is large, the condition number of the resulting system gets bigger resulting with a slow convergence. With the two-term disjoining pressure model we used, when the film thickness $f$ falls below the precursor film thickness$f_0$, the film is repelled from the substrate by the repulsive force. When $f = f_0$, $\Pi = 0$. Both the variation of disjoining pressure and its energy density have higher gradients for the pairs $(9,3)$ and $(4,3)$ compared with $(3,2)$ and they require better resolution, again with a slower convergence. A similar observation can be seen in Schwartz and Elley [50]. Because of these reasons, we use pair $(m, n) = (3,2)$.

The choice of $f_0$ also affects the solution. We check the effect of precursor film thickness by varying it from $f_0 = 0.01$ down to $f_0 = 0.0005$. The thicker precursor films do not predict the imposed contact angle while the one we used, $f_0 = 0.001$, predict the contact angle within an error of 1°. Going further below to $f_0 = 0.0005$ does not vary the profile, but it has slower convergence compared with $f_0 = 0.01$ as the Hamakar constant in the disjoining pressure scales as ${f_0}^{-1}$, which generates larger valuesv as $f_0$ becomes smaller. Therefore, we pick $f_0 = 0.001$.

# 3. NUMERICAL METHOD

## 3.1. Weak Formulation and Numerical Solution Procedure

To integrate the evolution equation given in equations (2.20-2.24), we use cubic finite element discretization in space and second order discretization in time. The evolution equation is valid in a domain $\Omega\colon 0 \leq x \leq L$. We approximate the test functions and $f$ from the same Hilbert-Sobolov space $\hat{\mathrm{H}}_1(\Omega)$. We first convert the film evolution equation into a set of two coupled equations, both being second order, by letting

$$\frac{\partial^2 f}{\partial x^2} - w = 0, \tag{3.1}$$

$$\frac{\partial f}{\partial t} + \frac{\partial}{\partial x}\begin{bmatrix} -f^3\left(Bo\left(\cos\alpha\dfrac{\partial(f+h)}{\partial x} - E\right)\right) - \dfrac{\partial w}{\partial x} \\ -\dfrac{\partial^3 h}{\partial x^3} - \dfrac{\partial \Pi}{\partial f}\dfrac{\partial f}{\partial x} \end{bmatrix} = 0. \tag{3.2}$$

We obtain the weak form of the set of equations (3.1-3.2) by first multiplying with corresponding test functions, namely $\overline{w}$ and $\bar{f}$, respectively; then integrating over the domain $\Omega$ and weakening the differentiability requirement using the fact that the test functions are chosen to be zero at any Dirichlet boundary condition:

$$\int_{\Omega} \frac{\partial f}{\partial x}\frac{\partial \overline{w}}{\partial x}\,dx + \int_{\Omega} w\overline{w}\,dx = 0, \tag{3.3}$$

$$\int_{\Omega} \frac{\partial f}{\partial t}\bar{f}\,d\Omega + \int_{\Omega} \begin{bmatrix} f^3\left(Bo\left(\cos\alpha\dfrac{\partial(f+h)}{\partial x} - E\right)\right) - \dfrac{\partial w}{\partial x} \\ -\dfrac{\partial^3 h}{\partial x^3} - \dfrac{\partial \Pi}{\partial f}\dfrac{\partial f}{\partial x} \end{bmatrix} \frac{\partial \bar{f}}{\partial x}\,d\Omega = 0. \tag{3.4}$$

We integrate in time using a second-order Crank-Nicolson scheme by setting the $\theta = 1/2$ on the standard $\theta$-scheme for the time $t \in (t^n, t^{n+1})$ and $\Delta t = t^{n+1} - t^n$ being the time step between the old time $t^n$ and the new time $t^{n+1}$ (see Appendix F).

The coupled equation in this scheme become,

$$\theta \begin{bmatrix} \displaystyle\int_\Omega \frac{\partial f^{n+1}}{\partial x}\frac{\partial \overline{w}}{\partial x}\,dx + \\ \displaystyle\int_\Omega w^{n+1}\overline{w}\,dx \end{bmatrix} + (1-\theta) \begin{bmatrix} \displaystyle\int_\Omega \frac{\partial f^{n}}{\partial x}\frac{\partial \overline{w}}{\partial x}\,dx + \\ \displaystyle\int_\Omega w^{n}\overline{w}\,dx \end{bmatrix} = 0 \tag{3.5}$$

$$\int \frac{f^{n+1} - f^n}{\Delta t}\bar{f}\,d\Omega$$

$$+\,\theta \left[\int_\Omega \begin{bmatrix} {f^{n+1}}^3 \left(Bo\left(\cos\alpha \dfrac{\partial (f^{n+1} + h)}{\partial x} - E\right)\right) - \dfrac{\partial w^{n+1}}{\partial x} \\ -\dfrac{\partial^3 h}{\partial x^3} - \dfrac{\partial \Pi^{n+1}}{\partial f^{n+1}}\dfrac{\partial f^{n+1}}{\partial x} \end{bmatrix} \frac{\partial \bar{f}}{\partial x}\,d\Omega\right]$$

$$+(1-\theta)$$

$$\left[\int_\Omega \begin{bmatrix} {f^{n}}^3 \left(Bo\left(\cos\alpha \dfrac{\partial (f^{n} + h)}{\partial x} - E\right)\right) - \dfrac{\partial w^{n}}{\partial x} \\ -\dfrac{\partial^3 h}{\partial x^3} - \dfrac{\partial \Pi^{n}}{\partial f^{n}}\dfrac{\partial f^{n}}{\partial x} \end{bmatrix} \frac{\partial \bar{f}}{\partial x}\,d\Omega\right] = 0 \tag{3.6}$$

We use piecewise continuous cubic shape functions $\phi^c$ for the space discretization. We approximate $f$, $w$ and corresponding test functions in isoparametric domain by

$$f^n = \sum {f_j}^n {\phi_j}^c,\ w^n = \sum {w_j}^n {\phi_j}^c,$$

$$f^{n+1} = \sum {f_j}^{n+1} {\phi_j}^c,\ w^{n+1} = \sum {w_j}^{n+1} {\phi_j}^c,$$

$$\bar{f} = \sum \bar{f}_i {\phi_i}^c,\ \ \bar{w} = \sum \bar{w}_i {\phi_i}^c. \tag{3.7}$$

Substituting approximations in equation (3.7) into the weak form equation (3.5-3.6) for all possible test functions, we obtain a system of the form $\boldsymbol{K}(u)u = \boldsymbol{R}$ to be solved for $u$, unknown vector comprising $f$ and $w$, and a residual vector of the unknown variables due to nonlinearity of the film evolution equation. We treat the nonlinearity at every time step using the Newton's method given in table 3.1.

**Table 3.1** Newton's Algorithm.

```
Newton's Algorithm Table
1:while $e > TOL$ do
    2: $\boldsymbol{u^{m+1}} = \boldsymbol{u^m} - \boldsymbol{T}(\boldsymbol{u^m})^{-1}\boldsymbol{r}(\boldsymbol{u^m})$
       $e = \|\boldsymbol{u^{m+1}} - \boldsymbol{u^m}\|$
    3: $\boldsymbol{u^{m+1}} = \boldsymbol{u^m}$
```

In this table, $\boldsymbol{r}$ is the residual vector and defined as $\boldsymbol{r}(\boldsymbol{u}) = \boldsymbol{K}(\boldsymbol{u})\boldsymbol{u} - \boldsymbol{R}$; $\boldsymbol{T}$ is the tangent stiffness matrix and defined as $\boldsymbol{T}(\boldsymbol{u}) = \frac{\partial \boldsymbol{r}}{\partial \boldsymbol{u}}$. We set the tolerance to be $10^{-12}$ in the Newton's iteration.

In figure 3.1, we show the convergence of the numerical method for the terminal shape of a droplet with $Bo = 0,\ \alpha = 0°,\ \theta_e = 15°$. The slopes of variation of two and infinity norm of errors with element size are around 3.5 as we use cubic finite element method.

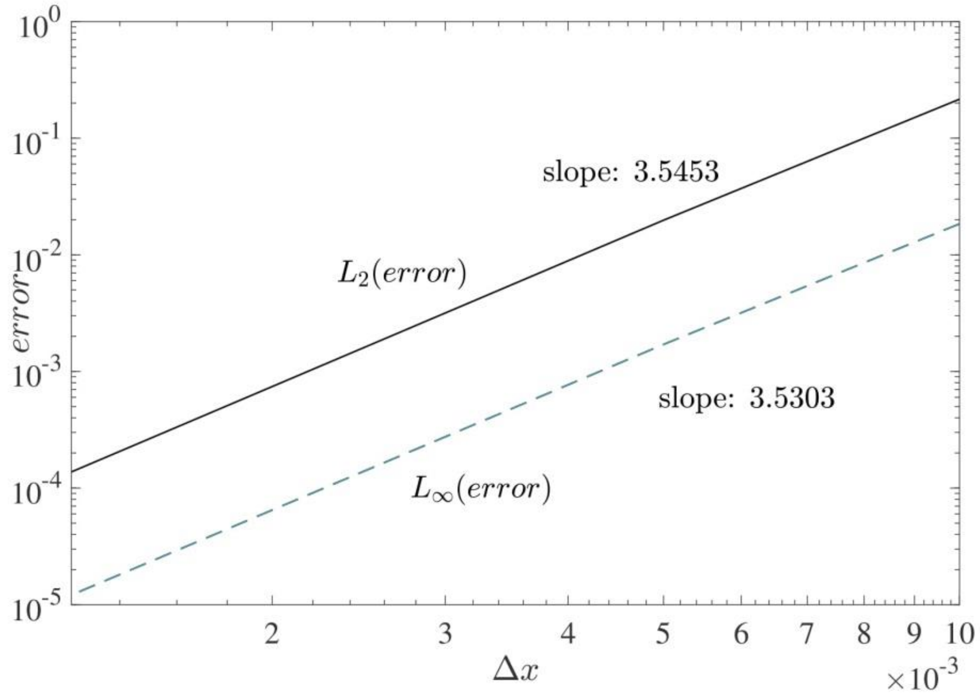

**Figure 3.1** Convergence of numerical method.

Time element size and element sizes are determined by the independence of solutions from both $\Delta t$ and $\Delta x$. We typically set $\Delta t$ to 0.0005 and vary the distance between each space node from 1/600 to 1/1800 depending on the resolution. We use 7th order Gauss rule of integration to compute all the integrals. The details of resulting system are given in Appendix E.

## 3.2 Numerical Method Validation: Droplet Motion on Flat Substrates

We devote this section to the validation of our solver analyzing droplet spreading over a flat horizontal surface and the motion of droplets over a flat inclined one.

### 3.2.1 Spreading Droplets

Tanner [60] and Mchale et al. [61] predict the motion of two-dimensional viscous oil drops over flat substrates. To a first approximation, the maximum droplet height decreases with time $t$ as $t^{-1/7}$; to show this relation, we put a circular arc droplet onto a flat substrate making an initial angle of $\theta = 15°$ and let it spread till the contact angle reaches zero for high-energy surface. In figure 3.2(*top*), we show the time history of maximum droplet height up to non-dimensional time of $t = 100$ and observe the same power-law relation after $t \sim 1$. Up to this time, the power-law relation does not hold because within this interval, the interface modifies itself to satisfy the evolution equation from an initially circular arc profile sitting over a flat precursor film of thickness $f_0$; a similar observation is made by Schwartz&Elley [50] for the early time over which the initial droplet shape matters.

We also check the dynamic variation of the advancing contact angle while the droplet spreads. When the droplet advances over an existing precursor film, the contact line is an apparent one, we measure it by finding locations of the maximum and minimum slopes of the droplet interface, draw a tangent line from this point the substrate and compute both angles and contact line positions where this line meets the substrate. The advancing contact angle differs from its Young value and is given as a function of $Ca$ by the Cox-Voinov model [35], [62]: ${\theta_A}^3 = {\theta_e}^3 - 9Caln(x/l_{micro})$ with $l_{micro}$ being a microscopic length-scale. This linear relationship between ${\theta_A}^3 - {\theta_e}^3$ and $Ca$, for the current spreading droplet is validated as shown in figure 3.2(*bottom*).

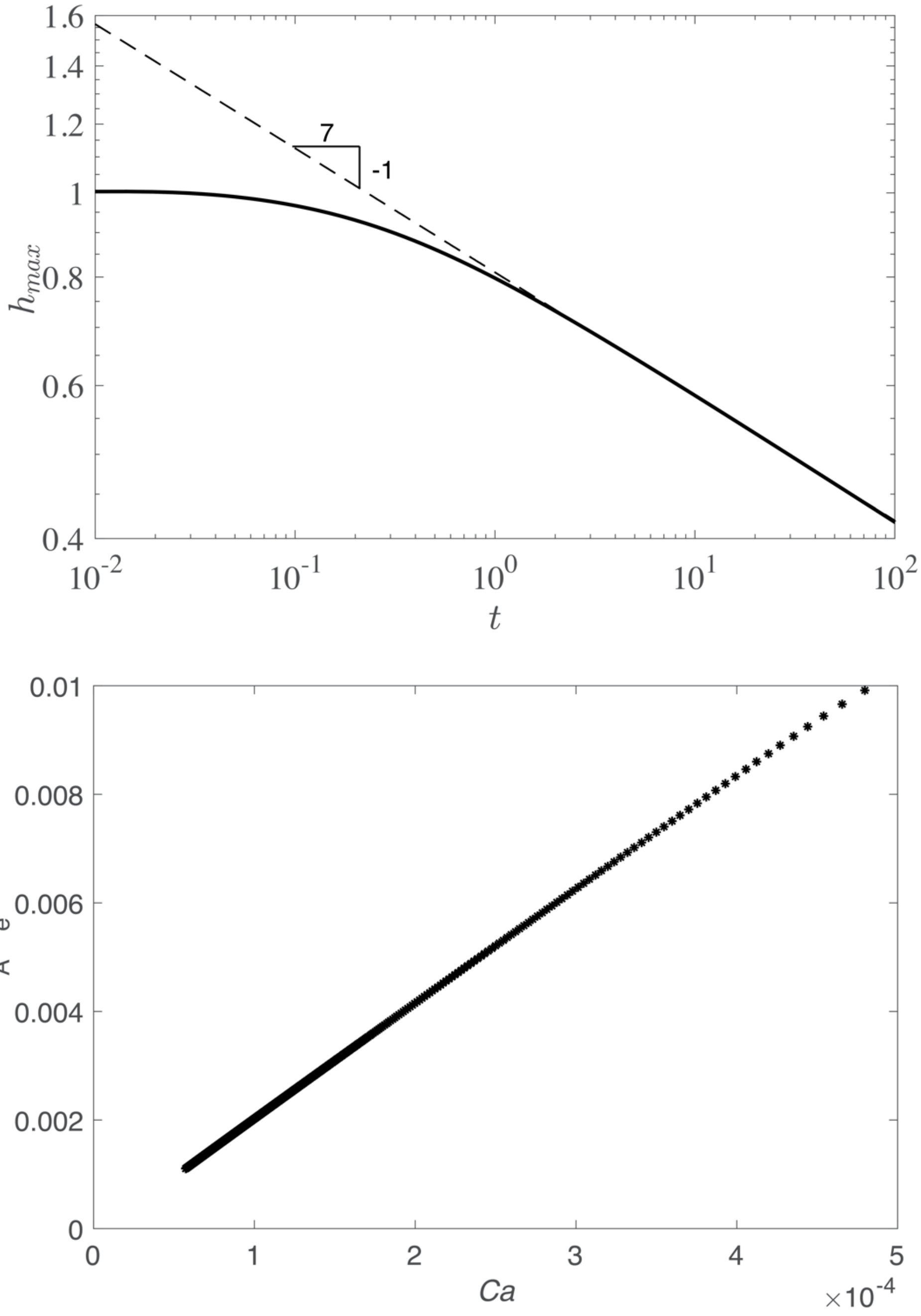

**Figure 3.2** (*top*) Time variation of maximum droplet height: two dimensional droplet spreading on a flat surface, see text for initial conditions; (*bottom*) speed of the advancing contact line of the spreading droplet.

### 3.2.2 Droplet Motion on Inclined Flat Substrates

When a droplet is driven by gravity over a flat inclined substrate, its shape does not remain circular at all times. Here, we show the droplet wetting transition over a flat inclined substrate. In all cases, we set $\theta_e$ to $10°$, $Bo$ to $0.75$ and vary the inclination angle $\alpha$ from $0°$ to $50°$, in $10°$ increments. As shown in figure 3.3, for small $Bo\sin\alpha$, droplet takes almost circular arc shape, surface tension forces determine the terminal shape. With increasing $Bo\sin\alpha$, however, the droplet elongates forming a tail shape toward the rear end; for all cases, the droplets move with constant speed after gaining their terminal shapes. Thiele et al. [40], Savva&Kalliadasis [41] and Park&Kumar [56] observe similar transitions. Though the terminal shapes can be predicted with a steady model by changing the reference frame moving with the terminal contact line speed, we do not include it here as our focus in this paper is the motion around the step.

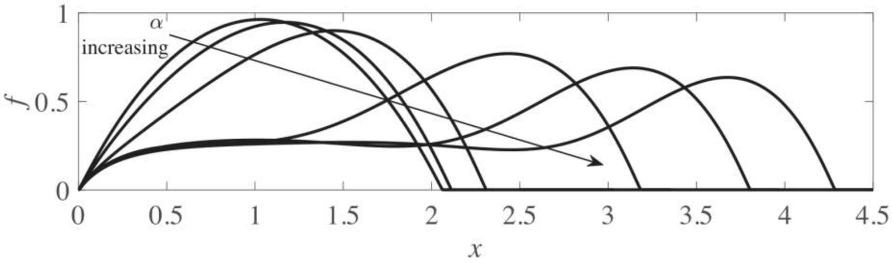

**Figure 3.3** Droplet wetting transition over an inclined flat substrate.

# 4. DROPLET MOTION AROUND INCLINED SINGLE STEP

While a droplet moves over a surface, the contact lines may pin and depin around structures. As we stated earlier, to be able to analyze the motion of moving contact lines around such structures, we simplify the substrate topography having a single backward facing step as shown in figure 2.1 to mimic a smooth roughness. This simple geometry provides us with a controllable slope with different step heights and steepness parameters.

We initialize the droplet motion by adding a circular arc droplet onto a precursor film thickness of $f_0$ away from the step. Here, we should note that the initial circular arc approximation of the droplet profile is unsteady and it takes some time to reach an equilibrium shape. However, for fixed volume, the pinning-depinning transition is not affected by the initial profile's circular arc approximation other than the one obtained by the terminal profile of an initially circular arc sitting on flat substrate although it affects the time taken until the transition around the step occurs. The initial location of the droplet center is at $x = 1.1$ whereas the step is located at $x = 2.6$. We consider a partial wetting fluid and set the equilibrium contact angle to $\theta_e = 15°$; this provides us with a slender droplet for which the long-wave approximation used in Chapter 2 is consistent.

Considering a three-dimensional droplet on an inclined flat substrate shown in figure 4.1 (*top*), the retention force parallel to the substrate can be computed by integrating the surface tension forces at the triple line along the contour of the droplet's contact with the substrate:

$$\boldsymbol{f}_{ret} = \oint_{CL} (\gamma_{lv}\cos\theta + \gamma_{sl} - \gamma_{sv})\boldsymbol{n}ds\,. \tag{4.1}$$

In the case of two-dimensional droplet shown in figure 4.1 (*middle*), equation (4.1) reduces to

$$\boldsymbol{f}_{ret} = -\gamma_{lv}(\cos\theta_R - \cos\theta_A)\boldsymbol{i}\,. \tag{4.2}$$

For a flat substrate as shown in figure 4.1 (*middle*), the critical condition for the onset of two-dimensional droplet motion occurs when

$$\gamma_{lv}(\cos\theta_R - \cos\theta_A) = \rho g A \sin\alpha_c\,. \tag{4.3}$$

The term on the left-hand side of equation (4.3) is the retention force due to hysteresis and the one on the right side is the gravitational force on the droplet acting in the direction of motion. A similar equation is given by Furmidge [28] and Macdougall&Ockrent [37]. Whenever $\alpha > \alpha_c$, the gravitational forces overcome the retention forces due to hysteresis and the droplet starts sliding.

On flat substrate, for a three-dimensional droplet symmetric with respect to $x$-axis and when $\oint_{CL} \boldsymbol{n} ds = 0$ or for a two-dimensional droplet, the lateral force contributions due to tensions $\gamma_{sl}$ and $\gamma_{sv}$ cancel for a chemically homogeneous substrate. That is not the case around the step (figure 4.1 (*bottom*)): there, the lateral force of $\gamma_{sv} - \gamma_{sl}$ at the receding contact line is bigger than the $x$-component of the force at the advancing contact line around the step which is $(\gamma_{sv} - \gamma_{sl})\cos\theta_{s,A}$ where $\theta_{s,A}$ is the angle of the step at the advancing contact line location measured from $x$-axis (see the magnified region at the bottom of figure (4.1)). Summation of these two, where we replace $\gamma_{sv} - \gamma_{sl}$ with $\gamma_{lv}\cos\theta_e$ by Young condition, results with an additional term due to existence of a step, and the balance between these retention forces and gravitational force determines the pinning and depinning of a droplet around the step:

$$\gamma_{lv}\left[\cos\theta_R - \cos\theta_A - \cos\theta_e\left(1 - \cos\theta_{s,A}\right)\right] \sim \rho g A \sin\alpha\,. \tag{4.4}$$

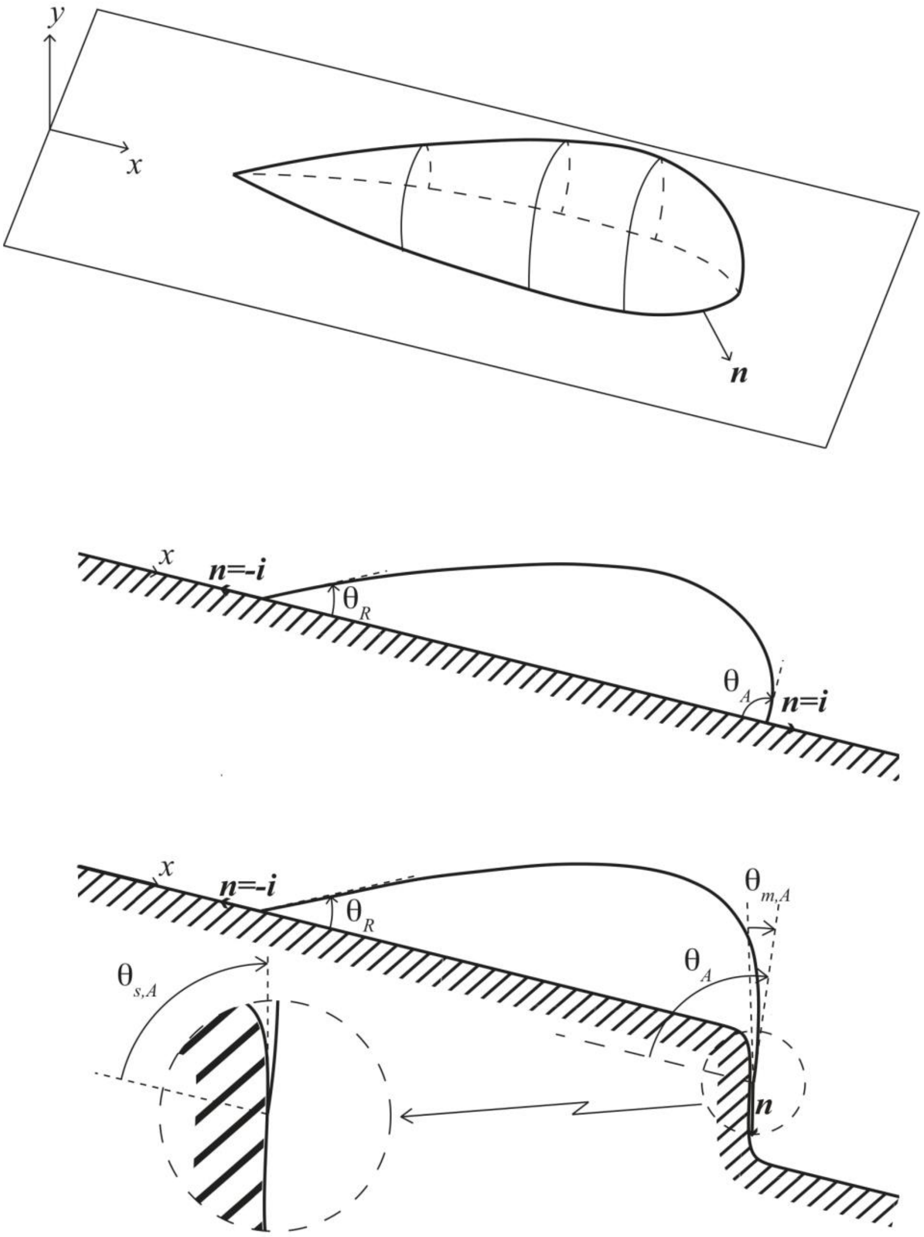

**Figure 4.1** (*top*) Three dimensional droplet sliding along inclined flat substrate, $\boldsymbol{n}$ is the outward unit normal at the contact line which is tangent to the substrate; two dimensional droplet sliding along inclined (*middle*) flat substrate, (*bottom*) step; $\boldsymbol{n}$ is the outward unit normal at the contact line which is tangent to the substrate. The step size is exaggerated compared with the droplet size to clarify the contact line region around the step.

The advancing contact angle $\theta_A$ is the summation of the step angle $\theta_{s,A}$ and mesoscopic angle $\theta_{m,A}$ at the advancing contact line which are measured at the length scale of the step topography. In equation (4.4), we assume that the receding contact line is away from the step, so that $\theta_{s,R} \to 0$. In the limit as $\theta_{s,A} \to 0$, the substrate is flat and $\theta_{m,A} = \theta_A$; we recover equation (4.3) when $\alpha = \alpha_c$.

To show that the balance given in equation (4.4) determines the pinning and depinning transition, we plot, in figure 4.2, the phase diagrams for three different steps. To form the diagrams, we run a set of numerical experiments in which we vary the $Bo$ and inclination angle $\alpha$ for fixed droplet volume of unity in each case. The dark shaded region is pinning region while the light one is the depinning region and the droplet follows a pinning-depinning transition determined by a curve shown with dashed lines in all cases that we obtain by the balance of retention forces and gravitational force given in equation (4.4). The existence of precursor film ahead of the contact lines changes the definition of the triple lines and the angles they make with the substrate. To guarantee that the balance is computed correctly, we construct the transition curve using the right-hand side of equation (4.4). This transition line shifts upwards as the step becomes steeper (from (*top*) to (*bottom*) in figure 4.2). The circular and triangular marks correspond respectively to pinned and depinned droplets around the step. For clarity, we also show some cases which are around the transition lines to emphasize that both varying the $\alpha$ for fixed $Bo$ and varying the $Bo$ for fixed $\alpha$ follow the transition.

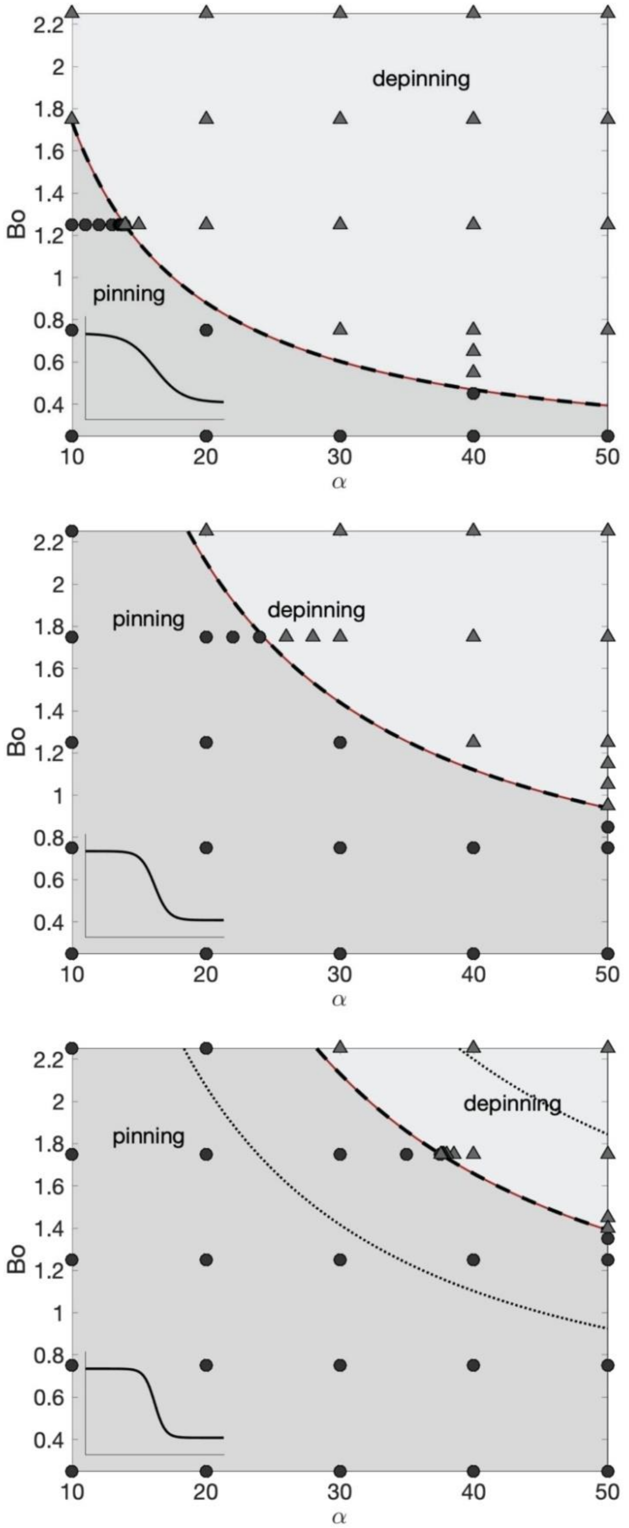

**Figure 4.2.** Phase diagrams of pinning-depinning transition of a two dimensional droplet around a step height $h_s = 0.05$: (*top*) $\lambda = 0.02$ (*middle*) $\lambda = 0.01$ (*bottom*) $\lambda = 0.075$; the seperators of the transitions shown as dashed black lines are obtained by plotting the force balance relation at the critical transition angle. The inclination angle $\alpha$ is in degrees. The insets show the step profile for the corresponding $\lambda$.

The retention force due to step is maximum whenever $\theta_{s,A}$ is maximum. This point corresponds to the middle of the step, namely the point at which its absolute slope is maximum. In figure 4.3($a$), the variation of the contact line location with $\alpha$, for fixed $Bo$, is shown. The advancing contact line pins around the step for $\alpha < \alpha_c$ and its location gets closer to the mid-point of the step at which the retention force due to it is maximum. It is clear from the inset that the contact line location approaches middle of the step as $\alpha \rightarrow \alpha_c$. A similar observation is made around a Gaussian shape defect [56].

The contribution of the step to the retention force due to the term $cos\theta_e\left(1 - \cos\theta_{s,A}\right)$ in equation (4.4) becomes more pronounced as the step becomes steeper. The changes in the receding contact angle with different steps is small compared with the changes at the advancing contact angle. This shows that the increase in the retention force with steeper step can be explained by a simple force balance around the advancing contact line. There, the magnitude of the upward retention force (in negative $\boldsymbol{i}$-direction) is

$$\left|\boldsymbol{f}_{ret,A}\right| = \gamma_{lv}\left(\cos\theta_A - \cos\theta_e \cos\theta_{s,A}\right). \tag{4.5}$$

As the step becomes steeper, both $\theta_A$ and $\theta_{s,A}$ increase in equation (4.5); however, the increase in $\theta_{s,A}$ is more pronounced compared with the increase in $\theta_A$, as well as $\cos\theta_{s,A}$ is multiplied with $\cos\theta_e < 1$, showing that the retention force increases with steeper step. This is simply observable by comparing the contributions of the terms to the retention force just before the depinning transition. We take three representative cases in which the droplets are pinned and they are located just before the pinning-depinning transition curves of three different $\lambda$ values (see figure 4.2(*top*) for $Bo = 1.25$, $\alpha = 13.95°$, figure 4.2(*middle*) for $Bo = 1.75$, $\alpha = 24°$ and figure 4.2(*bottom*) for $Bo = 1.75$, $\alpha = 37.52°$ ). We respectively measure the receding and advancing contact angles by calculating the maximum and minimum slopes of the interface $\zeta$ (these are the apparent angles; the contact line locations are at the points where a tangent line to the interface meets the substrate at the corresponding angle locations). The measured receding contact angle contribution to the retention force due to $\cos\theta_R$ remains nearly the same while advancing contact angle contribution increases as $\lambda$ increases and retention force due the step existence increases the hysteresis.

Up until the pinning occurs, the motion of the contact line is determined by the balance of viscous, capillary and retention forces. When we plot the advancing contact line locations, $x_{A,CL}$, against the time, they collapse onto each other when time is scaled with $Bo\sin\alpha$ as shown in figure 4.3($b$). The shaded region refers to the pinning while the other is the advancing of the contact line. This plot simply shows that the contact line Capillary number (based on contact line speed defined as $Ca = \eta V_{CL}/\gamma$) scales linearly with the $Bo\sin\alpha$ up to pinning (shaded area in figure 4.3($b$)). A similar experimental observation can be seen in figure 2 of Podgorski et al. [63]. The variation of $x$-coordinate of the droplet's center of gravity follows a similar pattern compared with $x_{A,CL}$ except its location slowly varies after the advancing contact line is pinned because the receding contact line is still moving towards right.

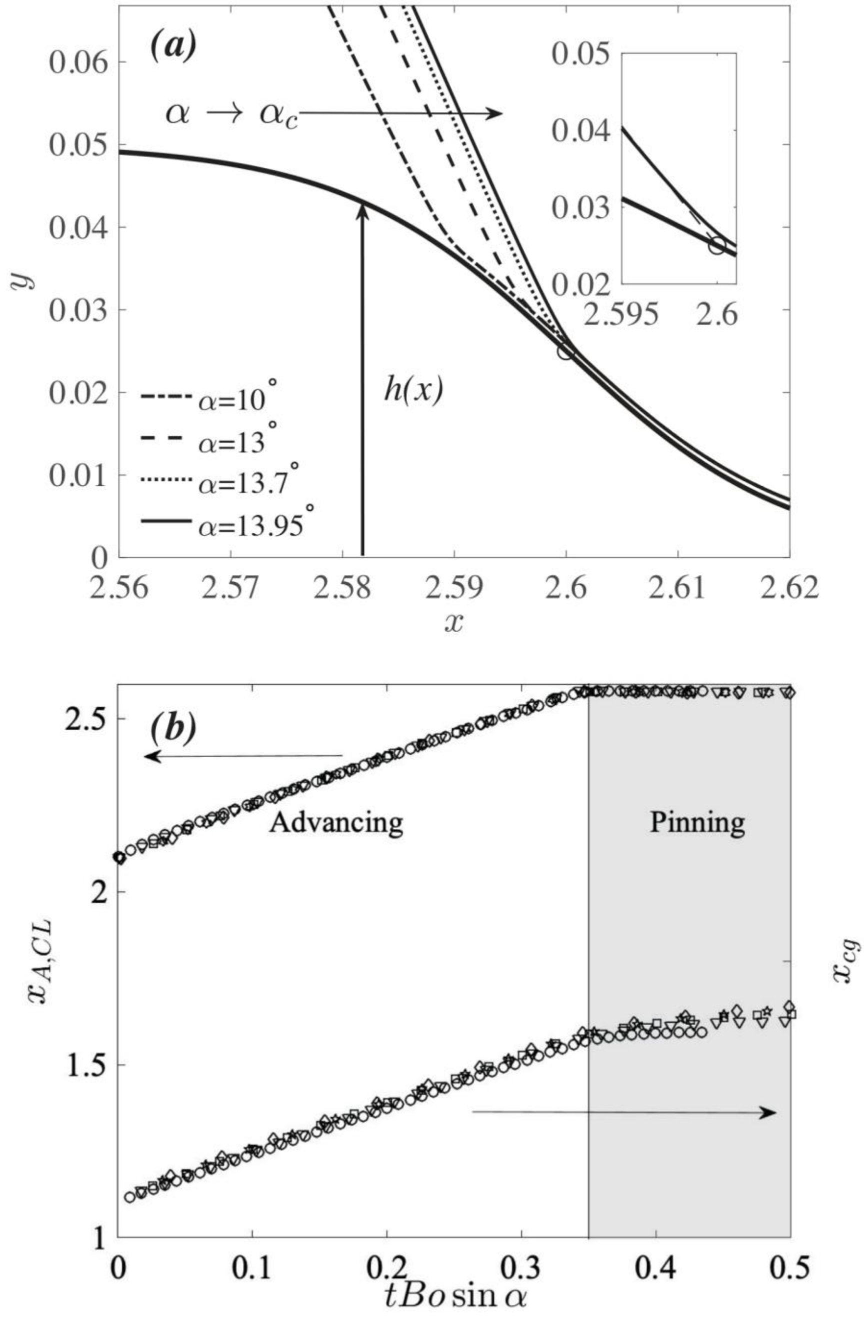

**Figure 4.3** ($a$) Pinned contact line locations as $\alpha \to \alpha_c$. We plot for $\alpha$ 10° to 13.95°, $Bo = 1.25$, $\theta_e = 15°$, $\lambda = 0.02$. The circle on the step locates the maximum $\theta_s$. The inset shows the contact line position for the critical case, the dashed line is tangent line drawn from the minimum slope of the interface near the advancing contact line; ($b$) position of the advancing contact line near the step (left axis), $x$-coordinate of the center of gravity of droplet (right axis which shares the same range with $x_{A,CL}$ ); $h_s = 0.05$, $\lambda = 0.01$, $Bo = 0.25$; ○: $\alpha = 10°$, ∇: $\alpha = 20°$, □: $\alpha = 30°$, ☆: $\alpha = 40°$, ◊: $\alpha = 50°$.

Though the phase diagrams are formed for three different step steepness parameter $\lambda$, varying $\lambda$ and/or step height $h_s$ determines the slope. The step is defined by equation (2.1) with its steepest point at $x_s$. At this point the absolute slope is maximum with the value $h_s/(2\lambda)$. Varying only the step height $h_s$ alters the slope; e.g. halving the step height from $h_s = 0.05$ to $h_s = 0.025$ halves the steepest slope. A case in which we set $Bo = 1.25$, $\alpha = 20°$ with $h_s = 0.05$ and $\lambda = 0.01$ pins at the step (see figure 4.2(*middle*)). For this case, we halve only the step height and the droplet depins. The full set of runs for the step heights $h_s = 0.025$ and $\lambda = 0.01$, 0.0075 reveal that we obtain the same phase diagrams given in figure 4.2(*top*) and (*middle*), respectively. It is the slope of the step that determines the pinning-depinning transition within the parameters studied. We should note here that if the height of the defect is sufficiently small, the droplet may not pin [57].

Varying the equilibrium contact angle, on the other hand, modifies the phase transitions as it determines the upper and lower bounds of the receding and advancing angles, respectively: $\theta_R \leq \theta_e \leq \theta_A$. For the steepest step geometry, we form the transition curves for two different equilibrium contact angles below and above the $\theta_e = 15°$: the dotted line in the dark shaded region of figure 4.2(*bottom*) is the transition curve obtained for $\theta_e = 10°$ while the dotted line inside the light shaded region is the transition curve obtained for $\theta_e = 20°$. The transition curve shifts upwards for a higher equilibrium contact angle as it is more difficult for the advancing contact line to move forward. The reverse is true for smaller contact angles; the transition curve is shifted downwards enlarging the depinning region as it is simpler for the advancing contact line to move.

# 5. EFFECT OF MULTIPLE STEPS

Over a rough surface, there exist step-ups and downs which alters the motion of the droplets. In this section, we mimic such a surface by combining the single step geometries to form substrates as shown in figure 5.1 with hatched region around $y = 0$.

In the analysis of the single step geometry, we assume that the receding contact line is away from the step. When the receding contact line encounters such a step, however, it alters the pinning-depinning transition because the mesoscopic angle of the receding contact line will be affected by the non-zero slope surfaces. In the case of a backward facing step, the substrate slope increases the mesoscopic angle of the receding contact line. The increase in the retention force alters the pinning depinning transition of the droplet. If a droplet pins at such a surface, its pinning-depinning transition is determined by the balance of contact line forces and gravitational forces given by

$$\gamma_{lv}\left[\cos\theta_R - \cos\theta_A - \cos\theta_e\left(\cos\theta_{s,R} - \cos\theta_{s,A}\right)\right] \sim \rho g A \sin\alpha\ . \tag{5.1}$$

Here $\theta_{s,R}$ is the substrate angle at the receding contact line and we recover equation (4.4) in the limit as $\theta_{s,R} \to 0$. The positive contribution to the retention force occurs around a step down where the pinning of the receding contact line is expected. While a step down increases the mesoscopic angle of the moving contact lines, the reverse reduces it which helps the contact line motion. Decreasing the slope of step-downs compared with the step ups helps the motion of droplet over such a rough substrate.

Figure 5.1 compares such an example. We take a representative droplet from the depinning region of the phase diagram shown in figure 4.2(*top*), namely we set $Bo = 0.75$ and $\alpha = 40°$. We, initially, place the droplet over the hills of the topography and let it slide. Different from the single step, the receding contact line alters the motion of the droplet. Making the backward-facing steps steeper (compare figure 5.1(*top*) and (*middle*)) impedes the motion. For a steeper backward facing step as shown in figure 5.1(*top*) compared with (*middle*), the receding contact line remains pinned longer at the steps.

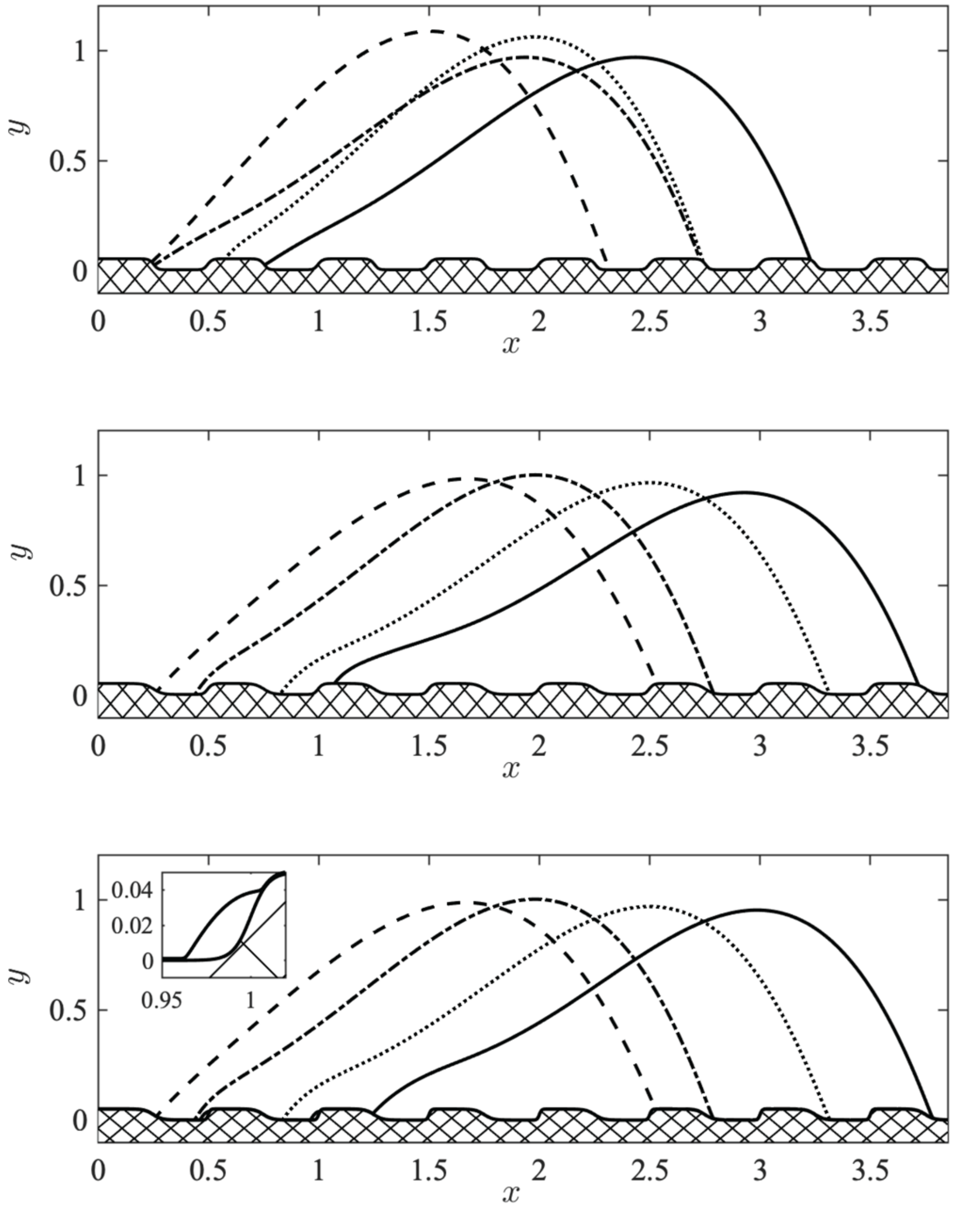

**Figure 5.1** Effect of substrate topography on the motion of droplet, (*top*) $\lambda = 0.02$ for both step-ups and downs, (*middle*) $\lambda = 0.04$ for step-downs and $\lambda = 0.02$ for step-ups, (*bottom*) $\lambda = 0.04$ for step-downs and $\lambda = 0.01$ for step-ups; $Bo = 0.75$, $\alpha = 40°$. Same line types correspond to the same time for comparison. The inset shows the residual droplet behind a forward-facing step.

For a sufficiently steep forward-facing steps, however, the receding contact line may leave a residual droplet behind the step as the film touches the step corner before the contact line is able to rise over it. It happens, for example, when we set $\lambda = 0.01$ or below at the forward-facing steps as shown in the inset of figure 5.1(*bottom*). Though the computed volume of the residual droplets proves to be small compared with the unit droplet volume, we show that, for fixed maximum slope of the forward-facing step, the volume increases monotonically with step height. We change the substrate design having different heights from the aforementioned design over which residual droplets formation is observed. Figure 5.2 shows the steps having heights $1.25h_s$ and $1.5h_s$ in ($a$), $1.75h_s$ and $2h_s$ in ($b$), $2.25h_s$ and $2.5h_s$ in ($c$) where $h_s = 0.05$. For fixed slope, the residual droplet volume increases as the step height increases. We plot, in figure 5.2($d$), the variation of residual droplet volume, $\upsilon_r$, as function of the step height. For similar substrate designs corresponding to figure 5.1($b$), we do not observe residual formation even at $2.5h_s$ because it is not only the step height which determines this formation but the slope of the steps.

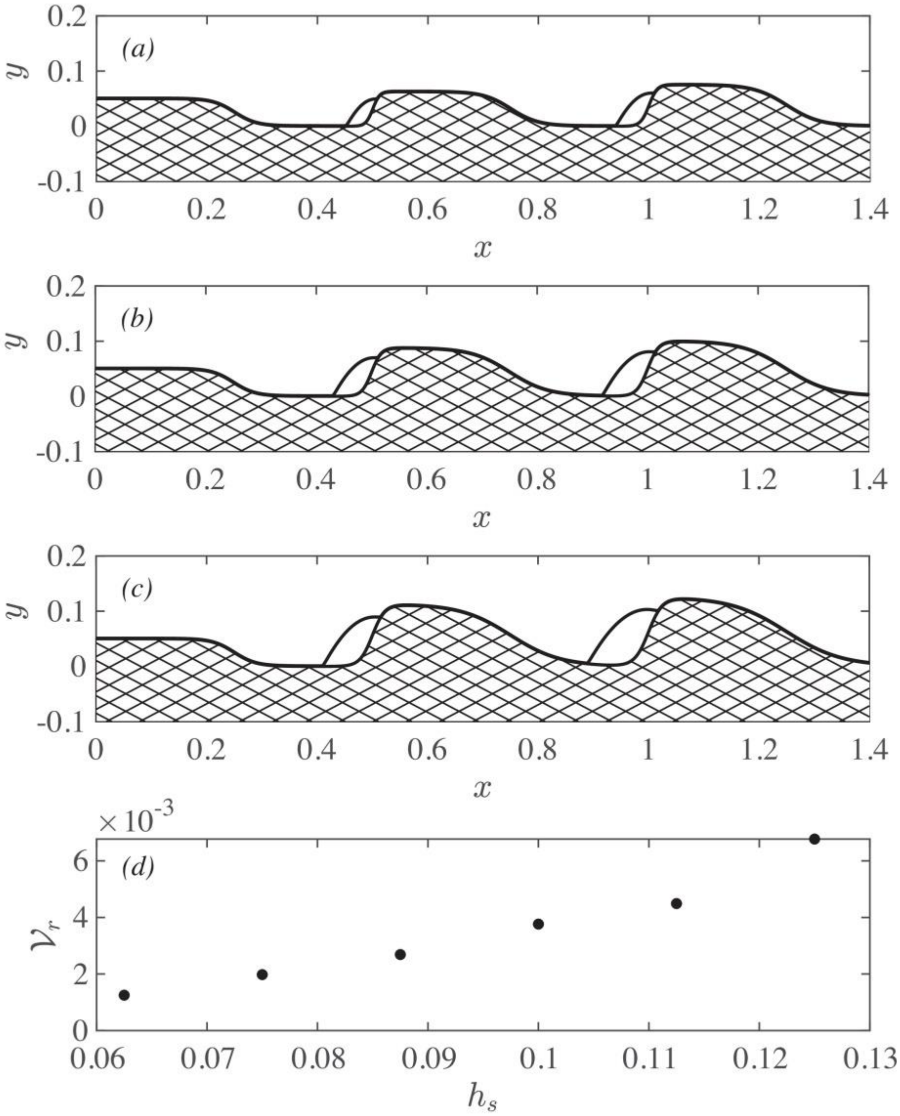

**Figure 5.2** Effect of step height on the residual droplet formation, (*a*) residual droplets behind step heights $h_s = 0.0625$ and $h_s = 0.075$, (*b*) residual droplets behind step of heights $h_s = 0.0875$ and $h_s = 0.1$, (*c*) residual droplets behind step of heights $h_s = 0.1125$ and $h_s = 0.125$, (*d*) residual droplet volume as a function of step height.

# 6. DEPINNING BY MULTIPLE DROPLETS

Coalescence of droplets is related to many industrial applications and natural phenomena such as printing processes, filtration, agricultural/industrial coatings, raindrop formation, collecting water in desert conditions, etc. In printing [6], for example, the resolution of the printed lines is determined by the coalescence dynamics of droplets while in agricultural coating processes coalescence of smaller spray droplets to larger ones ends up with an inefficient coating of the leaf surface [14]. It is observed that the coarsening by small droplet coalescence over inclined substrates is different than horizontal ones [64], [65]. In this section, we simply demonstrate how smaller droplet's coalescence into larger one changes the pinning-depinning transition.

For a certain volume droplet which is pinned at the step, the pinning-depinning transition can be shifted upwards by addition of a second droplet. This scenario can be thought fo as the depinning of droplets on a window of a rainy day which were initially stuck to the pane [66]. In all the cases forming the phase diagrams in figure 4.2, we set the volume of the droplet per unit depth to unity. When additional droplet is introduced into the domain, it slides down, meets first the receding contact line (its trailing edge) of the pinned droplet, then the two droplets coalesce and the new droplet is able to depin if the additional droplet volume is enough to shift the effective $Bo$ on the coalesced droplet into the depinning region. To show that, we consider one of the cases in which the droplet is pinned at the step. For example, the case of $Bo = 1.25$ and $\alpha = 50°$ is pinned as shown by the circle in figure 4.2(*bottom*) of the steepest step considered. For this droplet to depin at the same inclination angle, the corresponding $Bo$ should be greater than 1.40, i.e. an addition of a droplet of the $1/8^{th}$ volume of the pinned droplet would suffice to exceed this limit (${x_s}^2 \rightarrow 1.125$ making effective $Bo = 1.4062$). We assume that the previous droplet motion leaves no residual behind and the upstream droplet starts moving over the pre-existing precursor film thickness of $f_0$. In figure 6.1, we show the time history of the addition of a second droplet on the upstream and its coalescence with the pinned droplet. The coalescence helps depin because the effective $Bo$ on the coalesced droplet is big enough to overcome the retention forces due to hysteresis. Mori et al. [67] experimentally observe similar behavior.

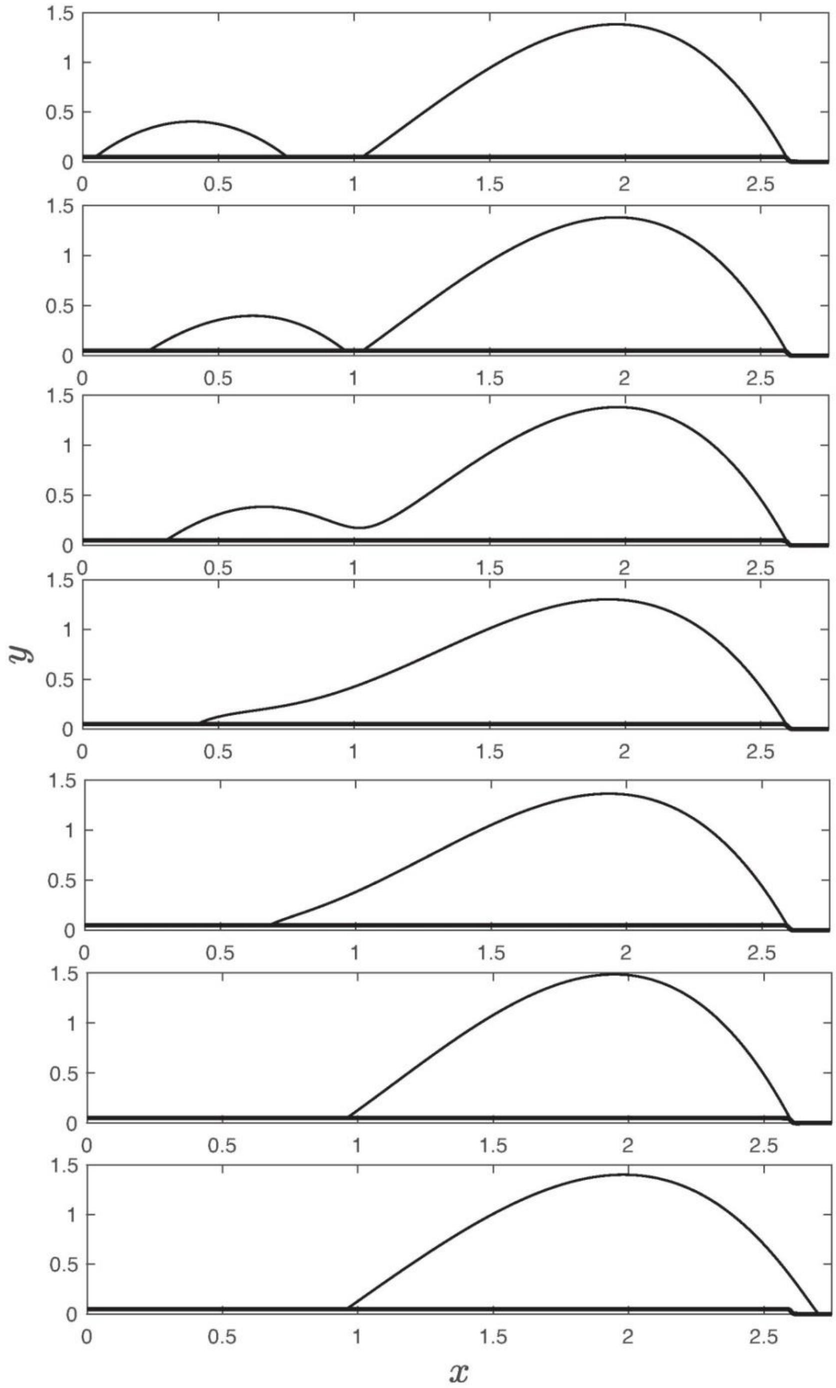

**Figure 6.1** Depinning by multiple droplets: time history of a droplet after coalescence from top to bottom; $Bo = 1.25$, $\alpha = 50°$, $\lambda = 0.0075$, see text for details.

# 7. CONCLUSION

We evaluate two dimensional droplet motion on an inclined and heterogeneous surface which includes single backward facing step or multiple steps in upward and downward direction for a partially wetting system. Structure of this solid surface cause contact angle hysteresis which includes deviation of contact angle from Young angle and pinning/depinning of droplet motion and droplet is pinned at the negative slope side of the solid surface physically, so we use single or multiple steps in order to demonstrate main physics of droplet motion. Our model problem is derived using lubrication theory and we obtain unsteady thin film evolution equation which is a fourth order nonlinear partial differential equation. Also we use precursor film approximation in order to remove the singularity ptoblem at the moving contact line. To integrate the governing equations, we have developed a cubic finite element solver and validate it against well known problems such as Tanner's law and Cox&Voinov equation.

The step geometry is determined by the step height and steepness parameter both determining its maximum absolute slope. The pinning of a droplet around a step simply shows that retention forces due surface energies dominate the gravitational forces and the balance between these determines the transition from a pinning to depinning regime. The phase diagrams obtained by numerical experiments clearly seperates this transition: a simple force balance of gravitational force acting on the droplet volume and the surface tension forces around the contact line defines this seperator above which the droplet depins from the step. The use of single backward facing step geometry helps explaining the increase in retention force due to step by a simple force balance argument made around the pinned contact line and for fixed $Bo$ and $\alpha$, we show that it is the slope of the step that determines this transition. Also we show that the existence of multiple steps may impede the motion of droplets becausе the receding contact line may pin at the backward-facing steps or leave residual droplet behind sufficiently steep forward facing steps and also we show that, for fixed slope the residual droplet volume increases with step height. At the end, we show that transition from pinning to deppinning of a droplet on a single backward facing step by adding a second droplet and coalesced droplet is depinned if effective $Bo$ achieves a critical value to overcome the retention forces.

The results contribute to the understanding of the pinning-depinning of contact lines around step-like heterogeneities. Our two-dimensional problem can be extended to other two/three dimensional models and would motivate further experiments and design of new surfaces.

# REFERENCES

1. Giles DK, Welsh A, Steinke WE, Saiz SG. Pesticide inhalation exposure, air concentration, and droplet size spectra from greenhouse fogging. Trans. Am. Soc. Agric. Eng. 1995; 38(5): 1321-1326.
2. Fürstner R, Barthlott W, Neinhuis C, Walzel P. Wetting and self-cleaning properties of artificial superhydrophobic surfaces. Langmuir. 2005; 21(3): 956-961.
3. Blossey R. Self-cleaning surfaces - Virtual realities. Nat. Mater. 2003; 2(5): 301-306.
4. Park J, Lim H, Kim W, Ko JS. Design and fabrication of a superhydrophobic glass surface with micro-network of nanopillars. J. Colloid Interface Sci. 2011; 360(1): 272-279.
5. Kuang M, Wang L, Song Y. Controllable Printing Droplets for High-Resolution Patterns. Adv. Mater. 2014; 26(40): 6950-6958.
6. Lee MW, Kim NY, Chandra S, Yoon SS. Coalescence of sessile droplets of varying viscosities for line printing. Int. J. Multiph. Flow. 2013; 56: 138-148.
7. Chung DCK, Katariya M, Huynh SH, Cheong BHP, Liew OW, Muradoglu MS, Ng TW. Uphill airflow transport of drops on superhydrophobic inclines. Colloids Interface Sci. Commun. 2015; 6: 1-4.
8. Rose JW. Dropwise condensation theory and experiment: A review. Proc. Inst. Mech. Eng. Part A. Power Energy. 2002; 216(2): 115-128.
9. Anand S, Paxson AT, Dhiman R, Smith JD, Varanasi KK. Enhanced condensation on lubricant-impregnated nanotextured surfaces. ACS Nano. 2012; 6(11): 10122-10129.
10. Bruckner AP, Mattick AT. High effectiveness liquid droplet/gas heat exchanger for space power applications. Acta Astronaut. 1984; 11(7-8): 519-526.
11. Gac JM, Jackiewicz A, Werner L, Jakubiak S. Consecutive filtration of solid particles and droplets in fibrous filters. Sep. Purif. Technol. 2016; 170: 234-240.
12. Trapaga G, Szekely J. Mathematical modeling of the isothermal impingement of liquid droplets in spraying processes. Metall. Trans. B. 1991; 22(6): 901-914.
13. Popinet S, Zaleski S, Núñez R. Coalescence of liquid drops by surface tension. Phys. Rev. E - Stat. Physics, Plasmas, Fluids, Relat. Interdiscip. Top. 2001; 63(4): 046309.
14. Mayo LC, Mccue SW, Moroney TJ, Forster WA, Kempthorne DM, Belward JA, Turner IW. Simulating droplet motion on virtual leaf surfaces. R. Soc. Open Sci. 2015; 2(5); 140528.
15. Wang JZ, Zheng ZH, Li HW, Huck WTS, Sirringhaus H. Dewetting of conducting polymer inkjet droplets on patterned surfaces. Nat. Mater. 2004; 3(3): 171-176.
16. Zhai L, Berg MC, Cebeci FC, Kim Y, Milwid JM, Rubner MF, Cohen RE. Patterned superhydrophobic surfaces: Toward a synthetic mimic of the namib desert beetle. Nano Lett. 2006; 6(6): 1213-1217.
17. Extrand CW, Moon SI. Repellency of the lotus leaf: Contact angles, drop retention, and sliding angles. Langmuir. 2014; 30(29): 8791-8797.
18. Gao X, Yan X, Yao X, Xu L, Zhang K, Zhang J, Yang B, Jiang L. The dry-style antifogging properties of mosquito compound eyes and artificial analogues prepared by soft lithography. Adv. Mater. 2007; 19(17): 2213-2217.

19. Cui Y, Li D, Bai H. Bioinspired Smart Materials for Directional Liquid Transport. Ind. Eng. Chem. Res. 2017; 56(17): 4887-4897.
20. Barthlott W, Mail M, Bhushan B, Koch K. Plant surfaces: Structures and functions for biomimetic innovations. Nano-Micro Lett. 2017; 9(2): 23.
21. Parker AR, Lawrence CR. Water capture by a desert beetle. Nature. 2001; 414(6589): 33.
22. Nørgaard T, Dacke M. Fog-basking behaviour and water collection efficiency in Namib Desert Darkling beetles. Front. Zool. 2010; 7(1): 23.
23. Tuteja A, Choi W, Ma M, Mabry JM, Mazzella SA, Rutledge GC, McKinley GH, Cohen RE. Designing superoleophobic surfaces. Science. 2007; 318(5856): 1618-1622.
24. Nosonovsky M, Bhushan B. Why re-entrant surface topography is needed for robust oleophobicity. Philos. Trans. R. Soc. Math. Phys. Eng. Sci. 2016; 374(2073): 20160185.
25. Liu T, Kim CJ. Turning a surface superrepellent even to completely wetting liquids. Science. 2014; 346(6213): 1096-1100.
26. Young T. III. An essay on cohesion of fluids. Philos. Trans. Soc. London. 1805; 95: 65-87.
27. De Gennes PG. Wetting: Statics and dynamics. Rev. Mod. Phys. 1985; 57(3): 827.
28. Furmidge CGL. Studies at phase interfaces. I. The sliding of liquid drops on solid surfaces and a theory for spray retention. J. Colloid Sci. 1962; 17(4): 309-324.
29. Bikerman JJ. Sliding of drops from surfaces of different roughnesses. J. Colloid Sci. 1950; 5(4): 349-359.
30. Espín L, Kumar S, Droplet spreading and absorption on rough, permeable substrates. J. Fluid Mech. 2015; 784: 465-486.
31. Zisman WA. Relation of the Equilibrium Contact Angle to Liquid and Solid Constitution. 1964; 1-51.
32. Wenzel RN. Resistance of solid surfaces to wetting by water. Ind. Eng. Chem. 1936; 28(8): 988-994.
33. Cassie ABD. Contact angles. Discussions of the Faraday Society. 1948; 3: 11-16.
34. Jiang Y, Xu W, Sarshar MA, Choi CH. Generalized models for advancing and receding contact angles of fakir droplets on pillared and pored surfaces. J. Colloid Interface Sci. 2019; 552: 359-371.
35. Cox RG. The dynamics of the spreading of liquids on a solid surface. Part 1. Viscous flow. J. Fluid Mech. 1986; 168: 169-194.
36. Voinov OV. Hydrodynamics of wetting. Fluid Dyn. 1976; 11(5): 714-721.
37. Macdougall G, Ockrent C. Surface energy relations in liquid/solid systems I. The adhesion of liquids to solids and a new method of determining the surface tension of liquids. Proc. R. Soc. London. Ser. A. Math. Phys. Sci. 1942; 180(981): 151-173.
38. Dussan EBV. On the ability of drops or bubbles to stick to non-horizontal surfaces of solids. Part 2. Small drops or bubbles having contact angles of arbitrary size. J. Fluid Mech. 1985; 151(1): 20.
39. Quéré D, Azzopardi MJ, Delattre L. Drops at rest on a tilted plane. Langmuir. 1998; 14(8): 2213-2216.
40. Thiele U, Neuffer K, Bestehorn M, Pomeau Y, Velarde MG. Sliding drops on an inclined plane. Colloids and Surfaces A: Physicochemical and Engineering Aspects. 2002; 206(1-3): 87-104.

41. Savva N, Kalliadasis S. Droplet motion on inclined heterogeneous substrates. J. Fluid Mech. 2013; 725: 462-491.
42. Huh C, Scriven LE. Hydrodynamic model of steady movement of a solid/liquid/fluid contact line. J. Colloid Interface Sci. 1971; 35(1): 85-101.
43. Dussan EB. On the Spreading of Liquids on Solid Surfaces: Static and Dynamic Contact Lines. Annu. Rev. Fluid Mech. 1979; 11(1): 371-400.
44. Hocking LM. The spreading of a thin drop by gravity and capillarity. *Q*. J. Mech. Appl. Math. 1983; 36(1): 55-69.
45. Hocking LM. Sliding and spreading of thin two-dimensional drops. Q. J. Mech. Appl. Math. 1981; 34(1): 37-55.
46. Dussan EBV, Davis SH. On the motion of a fluid-fluid interface along a solid surface. J. Fluid Mech. 1974; 65(1): 71-95.
47. Ruckenstein E, Dunn CS. Slip velocity during wetting of solids. J. Colloid Interface Sci. 1977; 59(1): 135-138.
48. Derjaguin B. A theory of capillary condensation in the pores of sorbents and of other capillary phenomena taking into account the disjoining action of polymolecular liquid films. Prog. Surf. Sci. 1992; 40(1-4): 46-61.
49. Teletzke GF, Davis HT, Scriven LE. Wetting hydrodynamics. Rev. Phys. Appl. 1988; 23(6): 989-1007.
50. Schwartz LW, Eley RR. Simulation of droplet motion on low-energy and heterogeneous surfaces. J. Colloid Interface Sci. 1998; 202(1): 173-188.
51. Pismen LM, and Pomeau Y. Disjoining potential and spreading of thin liquid layers in the diffuse-interface model coupled to hydrodynamics. Phys. Rev. E - Stat. Physics, Plasmas, Fluids, Relat. Interdiscip. Top. 2000; 62(2): 2480.
52. Hamaker HC. The London-van der Waals attraction between spherical particles. Physica. 1937; 4(10): 1058-1072.
53. Savva N, Kalliadasis S. Dynamics of moving contact lines: A comparison between slip and precursor film models. EPL. 2011; 94(6): 64004.
54. Sibley DN, Nold A, Savva N, Kalliadasis S. A comparison of slip, disjoining pressure, and interface formation models for contact line motion through asymptotic analysis of thin two-dimensional droplet spreading. J. Eng. Math. 2015; 94(1): 19-41.
55. Savva N, Kalliadasis S. Influence of gravity on the spreading of two-dimensional droplets over topographical substrates. J. Eng. Math. 2012; 73(1): 3-16.
56. Park J, Kumar S. Droplet Sliding on an Inclined Substrate with a Topographical Defect. Langmuir. 2017; 33(29): 7352-7363.
57. Kalinin YV, Berejnov V, Thorne RE. Contact line pinning by microfabricated patterns: Effects of microscale topography. Langmuir. 2009; 25(9): 5391-5397.
58. Dyson DC. Contact line stability at edges: Comments on Gibbs's inequalities. Phys. Fluids. 1988; 31(2): 229-232.
59. Escobar JME, Dietrich E, Arscott S, Zandvliet HJW, Zhang X, Lohse D. Zipping-Depinning: Dissolution of Droplets on Micropatterned Concentric Rings. Langmuir. 2018; 34(19): 5396-5402.
60. Tanner LH. The spreading of silicone oil drops on horizontal surfaces. J. Phys.-D. 1979; 12(9): 1473-1484.
61. Mchale G, Newton MI, Neil J. The spreading of small viscous stripes of oil role of topography. 1995; 28(9): 1925.
62. Voinov OV. Hydrodynamics of wetting. Fluid Dyn. 1976; 11(5): 714-721.

63. T. Podgorski, J. M. Flesselles, and L. Limat. Corners, cusps, and pearls in running drops. Phys. Rev. Lett. 2001; 87(3): 361021-361024.
64. Wilczek M, Tewes W, Engelnkemper S, Gurevich SV, Thiele U. Sliding Drops: Ensemble Statistics from Single Drop Bifurcations. Phys. Rev. Lett. 2017; 119(20): 204501.
65. Prabhala BR, Panchagnula MV, Vedantam S. Three-dimensional equilibrium shapes of drops on hysteretic surfaces. Colloid Polym.Sci. 2013; 291(2):279-289.
66. Quéré D. Fakir droplets. Nat. Mater. 2002; 1(1): 14-15.
67. Mori YH, van de Ven TGM, Mason SG. Resistance to spreading of liquids by sharp edged microsteps. Colloids and Surfaces. 1982; 4(1): 1-15.
68. London F. The general theory of molecular forces. Trans. Faraday Soc. 1937; 33: 8b-26.
69. Sokolov IY. Pseudo-non-contact mode: Why it can give true atomic resolution. Applied Surface Science. 2003; 210(1-2): 37-42.

# APPENDIX A: LONDON VAN DER WAALS FORCES

Hamakar compute London van der Waals forces between two sphere particles which includes $q$ atoms per their volume. Energy transmitted due to this interaction is evaluated theoretically and experimentally by London [68] and Sokolov [69] and expressed as:

$$E = -\int dV_1 \int \frac{q^2\lambda}{r^6} dV_2 \tag{A.1}$$

where $dV_1$ and $dV_2$ are selected differential volumes for spheres, $\lambda$ is London van der Waals constant and $r$ is distance between differential volumes. So he considers a sphere with a radius of $R_1$ and center point of $O$ and second sphere with a radius of $r$ and center point of $P$. This configuration is demonstrated by Hamakar [52] and in this configuration first sphere is cutted with second sphere and angle between perpendicular edge constituted surface from second sphere center point and one edge of second sphere is defined as $\theta_0$. So constituted surface can be formularized as:

$$S = 2\pi \int_0^{\theta_0} r^2 \sin\theta d\theta, \tag{A.2}$$

$${R_1}^2 = R^2 + r^2 - 2Rr\cos\theta_0, \tag{A.3}$$

$$S = \frac{\pi r}{R}\left({R_1}^2 - (R-r)^2\right). \tag{A.4}$$

Also London van der Waals potential energy for a single atom

$$E = -\int_{R-R_1}^{R+R_1} \frac{q\lambda}{r^6} \pi \frac{r}{R}\left({R_1}^2 - (R-r)^2\right) dr \approx -\frac{qr\lambda}{6}\frac{1}{r^3}. \tag{A.5}$$

Similarly London van der Waals potential energy for total amount of atom between two flat plates which includes a distance *d* is formulated as:

$$E \approx -\int_{d}^{\infty} \frac{q\lambda\pi}{6}\frac{1}{r^3} q dr \approx -\frac{q^2\pi\lambda}{12d^2} \approx -\frac{A}{12\pi}\frac{1}{d^2}, \tag{A.6}$$

and London van der Waals force can be computed by taking derivative of potential energy with respect to distance $d$ :

$$F_w = \frac{A}{6\pi}\frac{1}{d^3}. \tag{A.7}$$

Equation (A.7) shows that London van der Waals component of disjoining pressure is proprtional to $\frac{1}{d^3}$.

# APPENDIX B: LUBRICATION EQUATIONS

We rewrite equations (2.2-2.3) in their open form as

$$\frac{\partial \tilde{u}}{\partial \tilde{x}} + \frac{\partial \tilde{v}}{\partial \tilde{y}} = 0, \tag{B.1}$$

$$\rho \left( \frac{\partial \tilde{u}}{\partial \tilde{t}} + \frac{\partial \tilde{u}}{\partial \tilde{x}} \tilde{u} + \frac{\partial \tilde{u}}{\partial \tilde{y}} \tilde{v} \right) = - \frac{\partial \tilde{p}}{\partial \tilde{x}} + \rho g \sin\alpha + \eta \left( \frac{\partial^2 \tilde{u}}{\partial \tilde{x}^2} + \frac{\partial^2 \tilde{y}}{\partial \tilde{y}^2} \right), \tag{B.2}$$

$$\rho \left( \frac{\partial \tilde{v}}{\partial \tilde{t}} + \frac{\partial \tilde{v}}{\partial \tilde{x}} \tilde{u} + \frac{\partial \tilde{v}}{\partial \tilde{y}} \tilde{v} \right) = - \frac{\partial \tilde{p}}{\partial \tilde{y}} + \rho g \cos\alpha + \eta \left( \frac{\partial^2 \tilde{v}}{\partial \tilde{x}^2} + \frac{\partial^2 \tilde{v}}{\partial \tilde{y}^2} \right). \tag{B.3}$$

To nondimensionalize, we use the following length, velocity, time and pressure scales as follows:

$$\tilde{u} = u u^s, \tag{B.4}$$

$$\tilde{v} = v v^s, \tag{B.5}$$

$$\tilde{x} = x x^s, \tag{B.6}$$

$$\tilde{y} = y y^s, \tag{B.7}$$

$$\tilde{t} = t t^s = t \frac{x^s}{u^s}, \tag{B.8}$$

$$\tilde{p} = p p^s = p \frac{\eta u^s}{x^s}. \tag{B.9}$$

Putting scales into equation (B.1), we obtain

$$\frac{\partial(uu^s)}{\partial(xx^s)}+\frac{\partial(vv^s)}{\partial(yy^s)}=0 \tag{B.10}$$

Rearranging we obtain

$$\frac{\partial u}{\partial x}+\frac{v^s}{y^s}\frac{x^s}{u^s}\frac{\partial v}{\partial y}=0. \tag{B.11}$$

$v^s$ in equation (B.11) is determined by enforcing nondimensionalization laws as

$$v^s=\frac{y^s u^s}{x^s}. \tag{B.12}$$

Similarly, equation (B.2) can be rewritten as

$$\rho\left(\frac{\partial(uu^s)}{\partial(tt^s)}+\frac{\partial(uu^s)}{\partial(xx^s)}uu^s+\frac{\partial(uu^s)}{\partial(yy^s)}vv^s\right)=-\frac{\partial(pp^s)}{\partial(xx^s)}+\rho g\sin\alpha+$$

$$\eta\left(\frac{\partial^2(uu^s)}{\partial(xx^s)^2}+\frac{\partial^2(uu^s)}{\partial(yy^s)^2}\right) \tag{B.13}$$

$$\rho\left(\frac{u^s}{t^s}\frac{\partial u}{\partial t}+u^s\frac{u^s}{x^s}\frac{\partial u}{\partial x}u+\frac{u^s v^s}{y^s}\frac{\partial u}{\partial y}v\right)=-\frac{p^s}{x^s}\frac{\partial p}{\partial x}+\rho g\sin\alpha+$$

$$\eta\left(\frac{u^s}{x^{s2}}\frac{\partial^2 u}{\partial x^2}+\frac{u^s}{y^{s2}}\frac{\partial^2 u}{\partial y^2}\right) \tag{B.14}$$

Simplyfying we obtain

$$\frac{\rho {u^s}^2}{x^s}\left(\frac{\partial u}{\partial t}+\frac{\partial u}{\partial x}u+\frac{\partial u}{\partial y}v\right)=-\frac{p^s}{x^s}\frac{\partial p}{\partial x}+\rho g sin\alpha+$$

$$\frac{\eta u^s}{y^{s^2}}\left(\frac{y^{s^2}}{x^{s^2}}\frac{\partial^2 u}{\partial x^2}+\frac{\partial^2 u}{\partial y^2}\right). \tag{B.15}$$

If we multiply all sides of equation (B.15) with $\frac{y^{s^2}}{\eta u^s}$, we obtain

$$\frac{\rho u^s x^s}{\eta}\left(\frac{y^s}{x^s}\right)^2\left(\frac{\partial u}{\partial t}+\frac{\partial u}{\partial x}u+\frac{\partial u}{\partial y}v\right)=-\frac{p^s y^{s^2}}{x^s \eta u^s}\frac{\partial p}{\partial x}+\frac{y^{s^2}}{\eta u^s}\rho g sin\alpha +$$

$$\left(\frac{y^{s^2}}{x^{s^2}}\frac{\partial^2 u}{\partial x^2}+\frac{\partial^2 u}{\partial y^2}\right). \tag{B.16}$$

$\frac{\rho u^s x^s}{\eta}$ term in equation (B.16) expresses Reynolds number which is the ratio of viscous forces to inertial forces and inertial forces are negligible small according to viscous forces due to smaller droplet velocity and length scale, so Reynolds number is much smaller than 1. Also we know that $\frac{y^s}{x^s} \ll 1$ so we can neglect expressions which includes this term and equation (B.18) reduces to:

$$-\frac{p^s y^{s^2}}{x^s \eta u^s}\frac{\partial p}{\partial x}+\frac{y^{s^2}}{\eta u^s}\rho g sin\alpha+\frac{\partial^2 u}{\partial y^2}=0. \tag{B.17}$$

The pressure scale is determined to be

$$p^s=\frac{\eta u^s x^s}{y^{s^2}}. \tag{B.18}$$

If we put this term in equation (B.17), we obtain nondimensional form of equation (B.2) as

$$-\frac{\partial p}{\partial x}+\frac{y^{s^2}}{\eta u^s}\rho g sin\alpha+\frac{\partial^2 u}{\partial y^2}=0. \tag{B.19}$$

If we dimensionalize equation (B.19), we obtain

$$-\frac{\partial\left(\frac{\tilde{p}}{p^s}\right)}{\partial\left(\frac{\tilde{x}}{x^s}\right)}+\frac{{y^s}^2}{\eta u^s}\ \rho g \sin\alpha+\frac{\partial^2\left(\frac{\tilde{u}}{u^s}\right)}{\partial\left(\frac{\tilde{y}^2}{{y^s}^2}\right)}=0, \tag{B.20}$$

$$\frac{\partial\tilde{p}}{\partial\tilde{x}}=\rho g \sin\alpha+\eta\frac{\partial^2\tilde{u}}{\partial\tilde{y}^2}. \tag{B.21}$$

So, equation (B.2) is converted to equation (B.21) and if we apply same procedure on equation (B.3), we obtain

$$\frac{\partial\tilde{p}}{\partial\tilde{y}}+\rho g \cos\alpha=0. \tag{B.22}$$

# APPENDIX C: INTERFACIAL MOMENTUM BALANCE

We can define liquid-vapor interface as $\tilde{y} - \tilde{\zeta}$ and so, unit outward normal vector of droplet surface can be defined in terms of curl of this term and norm of the gradient of term in $\tilde{x}$ and $\tilde{y}$ direction.

$$\boldsymbol{n} = \frac{\tilde{\nabla}\left(\tilde{y} - \tilde{\zeta}(\tilde{x}, \tilde{t})\right)}{\left|\tilde{\nabla}\left(\tilde{y} - \tilde{\zeta}(\tilde{x}, \tilde{t})\right)\right|} \tag{C.1}$$

$$\tilde{\nabla}\left(\tilde{y} - \tilde{\zeta}(\tilde{x}, \tilde{t})\right) = \left(\frac{\partial}{\partial \tilde{x}}\boldsymbol{i} + \frac{\partial}{\partial \tilde{y}}\boldsymbol{j}\right)\left(\tilde{y} - \tilde{\zeta}(\tilde{x}, \tilde{t})\right) \tag{C.2}$$

$$\tilde{\nabla}\left(\tilde{y} - \tilde{\zeta}(\tilde{x}, \tilde{t})\right) = \frac{\partial}{\partial \tilde{x}}\left(\tilde{y} - \tilde{\zeta}(\tilde{x}, \tilde{t})\right)\boldsymbol{i} + \frac{\partial}{\partial \tilde{y}}\left(\tilde{y} - \tilde{\zeta}(\tilde{x}, \tilde{t})\right)\boldsymbol{j} \tag{C.3}$$

$$\tilde{\nabla}\left(\tilde{y} - \tilde{\zeta}(\tilde{x}, \tilde{t})\right) = \frac{\partial \tilde{y}}{\partial \tilde{x}}\boldsymbol{i} - \frac{\partial \tilde{\zeta}(\tilde{x}, \tilde{t})}{\partial \tilde{x}}\boldsymbol{i} + \frac{\partial \tilde{y}}{\partial \tilde{y}}\boldsymbol{j} - \frac{\partial \tilde{\zeta}(\tilde{x}, \tilde{t})}{\partial \tilde{y}}\boldsymbol{j} \tag{C.4}$$

In this equation, we know that upper boundary of the liquid-air interface varies with only $\tilde{x}$ location and time, so we apply this information to in this equation, we obtain

$$\tilde{\nabla}\left(\tilde{y} - \tilde{\zeta}(\tilde{x}, \tilde{t})\right) = -\frac{\partial \tilde{\zeta}(\tilde{x}, \tilde{t})}{\partial \tilde{x}}\boldsymbol{i} + \boldsymbol{j}, \tag{C.5}$$

and norm of this term is

$$\left|\tilde{\nabla}\left(\tilde{y} - \tilde{\zeta}(\tilde{x}, \tilde{t})\right)\right| = \sqrt{\left(\frac{\partial \tilde{\zeta}(\tilde{x}, \tilde{t})}{\partial \tilde{x}}\right)^2 + 1.} \tag{C.6}$$

Then unit normal is found to be

$$\boldsymbol{n} = \frac{\boldsymbol{j} - \frac{\partial \tilde{\zeta}(\tilde{x},\tilde{t})}{\partial \tilde{x}} \boldsymbol{i}}{\sqrt{\left(\frac{\partial \tilde{\zeta}(\tilde{x},\tilde{t})}{\partial \tilde{x}}\right)^2 + 1}} \tag{C.7}$$

We take divergence of $\boldsymbol{n}$, we obtain these results:

$$\widetilde{\nabla} \cdot \boldsymbol{n} = \left(\frac{\partial}{\partial \tilde{x}} \boldsymbol{i} + \frac{\partial}{\partial \tilde{y}} \boldsymbol{j}\right) \cdot \left( \frac{-\frac{\partial \tilde{\zeta}(\tilde{x},\tilde{t})}{\partial \tilde{x}}}{\sqrt{\left(\frac{\partial \tilde{\zeta}(\tilde{x},\tilde{t})}{\partial \tilde{x}}\right)^2 + 1}} \boldsymbol{i} + \frac{1}{\sqrt{\left(\frac{\partial \tilde{\zeta}(\tilde{x},\tilde{t})}{\partial \tilde{x}}\right)^2 + 1}} \boldsymbol{j} \right), \tag{C.8}$$

and rewrite as

$$\widetilde{\nabla} \cdot \boldsymbol{n} = \frac{\partial}{\partial \tilde{x}} \left( \frac{-\frac{\partial \tilde{\zeta}(\tilde{x},\tilde{t})}{\partial \tilde{x}}}{\sqrt{\left(\frac{\partial \tilde{\zeta}(\tilde{x},\tilde{t})}{\partial \tilde{x}}\right)^2 + 1}} \right) + \frac{\partial}{\partial \tilde{y}} \left( \frac{1}{\sqrt{\left(\frac{\partial \tilde{\zeta}(\tilde{x},\tilde{t})}{\partial \tilde{x}}\right)^2 + 1}} \right). \tag{C.9}$$

In this equation, second term of the right hand side equates to zero because upper boundary of the interface vary with only $\tilde{x}$ location and time, equation (C.9) then simplifies to

$$\widetilde{\nabla} \cdot \boldsymbol{n} = \frac{\partial}{\partial \tilde{x}} \left( \frac{-\frac{\partial \tilde{\zeta}(\tilde{x},\tilde{t})}{\partial \tilde{x}}}{\sqrt{\left(\frac{\partial \tilde{\zeta}(\tilde{x},\tilde{t})}{\partial \tilde{x}}\right)^2 + 1}} \right). \tag{C.10}$$

If we assume that droplet surface has a small slope, $\left(\frac{\partial \tilde{\zeta}(\tilde{x},\tilde{t})}{\partial \tilde{x}}\right)^2$ is much smaller than $\frac{\partial \tilde{\zeta}(\tilde{x},\tilde{t})}{\partial \tilde{x}}$, equation (C.10) simplifies to

$$\widetilde{\nabla} \cdot \boldsymbol{n} = -\frac{\partial^{\boldsymbol{2}} \tilde{\tilde{\zeta}}(\tilde{x}, \tilde{t})}{\partial \tilde{x}^2}. \tag{C.11}$$

# APPENDIX D: FILM EVOLUTION EQUATION

If we take derivative of volumetric flow rate per unit depth and apply Leibnitz theorem,

$$\frac{\partial \tilde{q}}{\partial \tilde{x}} = \frac{\partial}{\partial \tilde{x}} \int_{h}^{\tilde{\zeta}} \tilde{u}\, d\tilde{y} \tag{D.1}$$

$$\frac{\partial \tilde{q}}{\partial \tilde{x}} = \int_{h}^{\zeta} \frac{\partial \tilde{u}}{\partial \tilde{x}} d\tilde{y} + \tilde{u} \frac{\partial \tilde{\zeta}}{\partial \tilde{x}} \tag{D.2}$$

If we combine equation (D.2) and dimensional continuity equation, we obtain these equations:

$$\frac{\partial \tilde{u}}{\partial \tilde{x}} = -\frac{\partial \tilde{v}}{\partial \tilde{y}} \tag{D.3}$$

$$\frac{\partial \tilde{q}}{\partial \tilde{x}} = -\frac{\partial \tilde{v}}{\partial \tilde{y}} + \tilde{u} \frac{\partial \tilde{\zeta}}{\partial \tilde{x}} \tag{D.4}$$

and we can define liquid-air interface as a material, so its material derivative must be equal to zero.

$$\frac{d}{d\tilde{t}} \left( \tilde{y} - \left( \tilde{\zeta} - \tilde{h} \right)(\tilde{x}, \tilde{t}) \right) = 0 \tag{D.5}$$

$$\frac{d\tilde{y}}{d\tilde{t}} - \frac{\partial \left( \tilde{\zeta} - \tilde{h} \right)}{\partial \tilde{t}} - \tilde{u} \frac{\partial \left( \tilde{\zeta} - \tilde{h} \right)}{\partial \tilde{x}} = 0 \tag{D.6}$$

In equation (D.6) term of $\frac{d\tilde{y}}{d\tilde{t}}$ is the $y$-velocity of droplet, if this term is evaluated with kinematic relation and if we put this term into equation (D.6), we obtain

$$\frac{\partial(\tilde{\zeta} - \tilde{h})}{\partial \tilde{t}} = \tilde{v} - \tilde{u}\frac{\partial(\tilde{\zeta} - \tilde{h})}{\partial \tilde{x}}. \tag{D.7}$$

In this model problem $y$ velocity component is negligibly small compared with $x$ velocity component, so equation (D.7) and (D.4) becomes:

$$\frac{\partial}{\partial \tilde{t}}(\tilde{\zeta} - \tilde{h}) = -\tilde{u}\frac{\partial(\tilde{\zeta} - \tilde{h})}{\partial \tilde{x}} \tag{D.8}$$

$$\frac{\partial \tilde{q}}{\partial \tilde{x}} = \tilde{u}\frac{\partial(\tilde{\zeta} - \tilde{h})}{\partial \tilde{x}} \tag{D.9}$$

and if we combine these two equations using $\tilde{f} = \tilde{\zeta} - \tilde{h}$, we obtain unsteady film evolution equation:

$$\frac{\partial \tilde{f}}{\partial \tilde{t}} + \frac{\partial \tilde{q}}{\partial \tilde{x}} = 0. \tag{D.10}$$

# APPENDIX E: RESULTING SYSTEM

If we put FEM approximations into the weak form equation (3.15-3.16), we obtain

$$\theta\begin{bmatrix}\int\limits_{\Omega}\frac{\partial}{\partial x}\left(\sum f_j{}^{n+1}\phi_j{}^c\right)\frac{\partial}{\partial x}\left(\sum \bar{w}_i\phi_i{}^c\right)dx+\\ \int\limits_{\Omega}\left(\sum w_j{}^{n+1}\phi_j{}^c\right)\left(\sum \bar{w}_i\phi_i{}^c\right)dx\end{bmatrix}+$$

$$(1-\theta)\begin{bmatrix}\int\limits_{\Omega}\frac{\partial}{\partial x}\left(\sum f_j{}^{n}\phi_j{}^c\right)\frac{\partial}{\partial x}\left(\sum \bar{w}_i\phi_i{}^c\right)dx+\\ \int\limits_{\Omega}\left(\sum w_j{}^{n}\phi_j{}^c\right)\left(\sum \bar{w}_i\phi_i{}^c\right)dx\end{bmatrix}=0, \tag{E.1}$$

$$\int\frac{\left(\sum f_j{}^{n+1}\phi_j{}^c\right)-\left(\sum f_j{}^{n}\phi_j{}^c\right)}{t^{n+1}-t^{n}}\left(\sum \bar{f}_i\phi_i{}^c\right)d\Omega+$$

$$\theta\left[\int\limits_{\Omega}\begin{bmatrix}\left(\sum f_j{}^{n+1}\phi_j{}^c\right)^3\\ \left(Bo\left(\cos\alpha\frac{\partial}{\partial x}\left(\sum\left(f_j{}^{n+1}\phi_j{}^c\right)+h\right)\right)-E\right)\\ -\frac{\partial}{\partial x}\left(\sum w_j{}^{n+1}\phi_j{}^c\right)-\frac{\partial^3 h}{\partial x^3}-\frac{\partial\left(\sum \Pi_j{}^{n+1}\phi_j{}^c\right)}{\partial\left(\sum f_j{}^{n+1}\phi_j{}^c\right)}\frac{\partial}{\partial x}\\ \left(\sum f_j{}^{n+1}\phi_j{}^c\right)\end{bmatrix}\frac{\partial\bar{f}}{\partial x}d\Omega\right]+$$

$$(1-\theta)\left[\int\limits_{\Omega}\begin{bmatrix}\left(\sum f_j{}^{n}\phi_j{}^c\right)^3\\ \left(Bo\left(\cos\alpha\frac{\partial}{\partial x}\left(\sum\left(f_j{}^{n}\phi_j{}^c\right)+h\right)\right)-E\right)\\ -\frac{\partial}{\partial x}\left(\sum w_j{}^{n}\phi_j{}^c\right)-\frac{\partial^3 h}{\partial x^3}\\ -\frac{\partial\left(\sum \Pi_j{}^{n}\phi_j{}^c\right)}{\partial\left(\sum f_j{}^{n}\phi_j{}^c\right)}\frac{\partial}{\partial x}\left(\sum f_j{}^{n}\phi_j{}^c\right)\end{bmatrix}\frac{\partial\bar{f}}{\partial x}d\Omega\right]=0. \tag{E.2}$$

We take summations outside of the integrals in equation (E.1-E.2) to obtain

$$\theta\left(\sum f_j{}^{n+1}\sum \bar{w}_i\int \frac{\partial \phi_j{}^c}{\partial x}\frac{\partial \phi_i{}^c}{\partial x}dx\right)+$$

$$\theta\left(\sum w_j{}^{n+1}\sum \bar{w}_i\int \phi_j{}^c\phi_i{}^c\,dx\right)+$$

$$(1-\theta)\left(\sum f_j{}^{n}\sum \bar{w}_i\int \frac{\partial \phi_j{}^c}{\partial x}\frac{\partial \phi_i{}^c}{\partial x}dx\right)+$$

$$(1-\theta)\left(\sum w_j{}^{n}\sum \bar{w}_i\int \phi_j{}^c\phi_i{}^c\,dx\right)=0 \tag{E.3}$$

$$\sum f_j{}^{n+1}\sum \bar{f}_i\int_\Omega \phi_i{}^c\phi_j{}^c d\Omega-\sum f_j{}^{n}\sum \bar{f}_i\int_\Omega \phi_i{}^c\phi_j{}^c d\Omega+$$

$$\theta\Delta t\sum f_j{}^{n+1}\sum \bar{f}_i\int_\Omega\left(\sum f_j{}^{n+1}\phi_j{}^c\right)^3\left(Bo\left(\cos\alpha\frac{\partial\left(\phi_j{}^c+h\right)}{\partial x}\right)\right)$$

$$\frac{\partial \phi_i{}^c}{\partial x}d\Omega-\theta\Delta t\sum f_j{}^{n+1}\sum \bar{f}_i$$

$$\int_\Omega\left(\sum f_j{}^{n+1}\phi_j{}^c\right)^2\phi_j{}^c\frac{\partial \phi_i{}^c}{\partial x}(BoE)d\Omega$$

$$-\sum w_j{}^{n+1}\sum \bar{f}_i\int \frac{\partial \phi_i{}^c}{\partial x}\frac{\partial \phi_j{}^c}{\partial x}d\Omega-\sum \bar{f}_i\int \frac{\partial \phi_i{}^c}{\partial x}\frac{\partial^3 h}{\partial x^3}d\Omega-$$

$$\frac{\sum \Pi_j{}^{n+1}}{\sum f_j{}^{n+1}}\sum f_j{}^{n+1}\sum \bar{f}_i\int \frac{\partial \Pi^{n+1}}{\partial f^{n+1}}\frac{\partial \phi_i{}^c}{\partial x}\frac{\partial \phi_j{}^c}{\partial x}d\Omega+(1-\theta)\Delta t$$

$$\sum f_j{}^n \sum \bar{f_i} \int_\Omega \left(\sum f_j{}^n \phi_j{}^c\right)^3 \left(Bo\left(\cos\alpha \frac{\partial\left(\phi_j{}^c + h\right)}{\partial x}\right)\right)$$

$$\frac{\partial \phi_i{}^c}{\partial x} \mathrm{d}\Omega - (1-\theta)\Delta t \left(\sum f_j{}^n\right) \sum \bar{f_i}$$

$$\int_\Omega \left(\sum f_j{}^n \phi_j{}^c\right)^2 \phi_j{}^c \frac{\partial \phi_i{}^c}{\partial x} (BoE) d\Omega -$$

$$\sum w_j{}^n \sum \bar{f_i} \int \frac{\partial \phi_i{}^c}{\partial x} \frac{\partial \phi_j{}^c}{\partial x} d\Omega - \sum \bar{f_i} \int \frac{\partial \phi_i{}^c}{\partial x} \frac{\partial^3 h}{\partial x^3} d\Omega -$$

$$\frac{\sum \Pi_j{}^n}{\sum f_j{}^n} \sum f_j{}^n \sum \bar{f_i} \int \frac{\partial \Pi^n}{\partial f^n} \frac{\partial \phi_i{}^c}{\partial x} \frac{\partial \phi_j{}^c}{\partial x} d\Omega = 0 \tag{E.4}$$

We define special expressions for integrals:

$$K_{ij} = \int_\Omega \frac{\partial \phi_j{}^c}{\partial x} \frac{\partial \phi_i{}^c}{\partial x} d\Omega \tag{E.5}$$

$$L_{ij} = \int_\Omega \phi_j{}^c \phi_i{}^c \, d\Omega \tag{E.6}$$

$$M_{ij} = \int_\Omega \left(\sum f_j{}^{n+1} \phi_j{}^c\right)^2 \phi_j{}^c \frac{\partial \phi_i{}^c}{\partial x} d\Omega \tag{E.7}$$

$$N_{ij} = \int_\Omega \left(\sum f_j{}^{n+1} \phi_j{}^c\right)^3 \phi_j{}^c \frac{\partial \phi_i{}^c}{\partial x} d\Omega \tag{E.8}$$

$$O_{ij} = \int_\Omega \frac{\partial \Pi}{\partial f} \frac{\partial \phi_i{}^c}{\partial x} \frac{\partial \phi_j{}^c}{\partial x} d\Omega \tag{E.9}$$

If we put these terms in equation (E.3-E.4), we simplify rewrite

$$\theta\left(\sum {f_j}^{n+1}\sum \overline{w}_i\, K_{ij}\right) + \theta\left(\sum {w_j}^{n+1}\sum \overline{w}_i L_{ij}\right) +$$

$$(1-\theta)\left(\sum {f_j}^{n}\sum \overline{w}_i K_{ij}\right) + (1-\theta)\left(\sum {w_j}^{n} L_{ij}\right) = 0, \tag{E.10}$$

$$\sum {f_j}^{n+1}\sum \bar{f}_i\, L_{ij} - \sum {f_j}^{n}\sum \bar{f}_i\, L_{ij} +$$

$$\theta\Delta t\sum {f_j}^{n+1}\sum \bar{f}_i\, Bo\cos\alpha N_{ij} - \theta\Delta t$$

$$\sum {f_j}^{n+1}\sum \bar{f}_i\, BoEM_{ij} - \sum {w_j}^{n+1}\sum \bar{f}_i\, K_{ij} -$$

$$-\frac{\sum {\Pi_j}^{n+1}}{\sum {f_j}^{n+1}}\sum {f_j}^{n+1}\sum \bar{f}_i\, O_{ij} +$$

$$(1-\theta)\Delta t\sum {f_j}^{n+1}\sum \bar{f}_i\, Bo\cos\alpha N_{ij} - (1-\theta)\Delta t$$

$$\sum {f_j}^{n}\sum \bar{f}_i\, BoEM_{ij} - \sum {w_j}^{n}\sum \bar{f}_i\, K_{ij} -$$

$$-\frac{\sum {\Pi_j}^{n}}{\sum {f_j}^{n}}\sum {f_j}^{n}\sum \bar{f}_i\, O_{ij} = 0. \tag{E.11}$$

The resulting system is

$$\begin{bmatrix} S_{ij} & -\theta\Delta t K_{ij} \\ K_{ij} & L_{ij} \end{bmatrix}\begin{bmatrix} f \\ w \end{bmatrix} = [R] \tag{E.12}$$

where $S_{ij} = L_{ij} + \theta\Delta tBo\cos\alpha N_{ij} - \theta\Delta tBoEM_{ij} + \theta\Delta tO_{ij}$ and $R = {f_j}^n K_{ij}$.

The unknown vector $u$ is

$$u = \begin{bmatrix} f \\ w \end{bmatrix}. \tag{E.13}$$

We solve this non-linear system by Newton's method and define residual as

$$r(\boldsymbol{u}) = S_{ij}(\boldsymbol{u})\boldsymbol{u} - R. \tag{E.14}$$

In the Newton's iteretion method, root of a any function is obtained by drawing a tangent line at the intersect point of function with axis and this process is repeated by taking new point as intersect point at the previous step and it is shown that this points approaches the root of the function gradually, so this relation formulated by

$$u^{k+1} = u^k - \frac{r(u^k)}{\frac{\partial r(u^k)}{\partial u}} \tag{E.15}$$

where $k$ and $k+1$ are the Newton iteration at the old and new step, respectively. Also we can define a tangent stiffness matrix as

$$\boldsymbol{T} = \frac{\partial r(u^k)}{\partial u}. \tag{E.16}$$

Then equation (E.15) turns into

$$u^{k+1} = u^k - \boldsymbol{T}^{-1} r(u^k). \tag{E.17}$$

We continue iteration until until difference between value of unknowns at old and new Newton itereation step is less than a tolerance.

$$\left||u^{k+1} - u^k|\right| < TOL \tag{E.18}$$

We set the tolerance to be $10^{-12}$.

# APPENDIX F: ORDER OF TIME INTEGRATION

We integrate in time using Cranck-Nickolson method which is a second order time integration method. We integrate an equation of the form which is expressed by

$$\frac{\partial f}{\partial t} = F(x,t) \tag{F.1}$$

and using standard $\theta$-scheme we approximate above (without considering the space discretization as this Appendix is devoted to the order of time integration)

$$\frac{f^{n+1} - f^{n}}{\Delta t} = \theta F(x, t^{n+1}) + (1-\theta) F(x, t^{n}). \tag{F.2}$$

The local truncation error in this approxiamation is then

$$\tau(x,t) = \frac{f^{n+1} - f^{n}}{\Delta t} - \theta F(x, t^{n+1}) - (1-\theta) F(x, t^{n}). \tag{F.3}$$

If we expand $f^{n+1}$ and $f^{n}$ into Taylor series around $t^{n}$, we obtain

$$f^{n+1} = f^{n} + \Delta t \frac{\partial f}{\partial t} + \frac{\Delta t^2}{2} \frac{\partial^2 f}{\partial t^2} + O(\Delta t^3),$$

$$F(x, t^{n+1}) = F(x, t^{n}) + \Delta t \frac{\partial F}{\partial t} + \frac{\Delta t^2}{2} \frac{\partial^2 F}{\partial t^2} + O(\Delta t^3). \tag{F.4}$$

If we put these terms into the error definition with replacing $\frac{\partial f}{\partial t}$ with $F$ from the equation (F.1), we obtain

$$\tau(x,t) = \Delta t \frac{\partial}{\partial t}\left(\frac{1}{2} F - \theta F\right) + O(\Delta t^2). \tag{F.5}$$

When $\theta = 1/2$, order $\Delta t$ terms are killed, so the Cranck-Nickolson method is $O(\Delta t^2)$.

# CURRICULUM VITAE

## Contact Information

Name: Aslı TİKTAŞ

E-mail: asli.tiktas@ahievran.edu.tr

## Education:

Since 2018: Master’s degree in mechanical engineering from university” İzmır Katip Çelebi University”, İzmir

2013-2017: Bachelor degree in mechanical engineering from university “Karadeniz Technical University”, Trabzon

## Academic Positions:

Since 2019: Research assistant at Kırşehir Ahi Evran University

## List of Publications:

Ceyhan U, Tiktaş A, Özdoğan M. Pinning and Depinning of Wenzel State Droplets Around Inclined Steps. Colloid and Interface Science Communications, March 2020; 35 (100238).